Mechanisms and rates of pyrite formation from hydrothermal fluid revealed by iron isotopes

Gleb S Pokrovski, Marc Blanchard, Gaëlle Saunier, Franck Poitrasson

Journal Pre-proofs

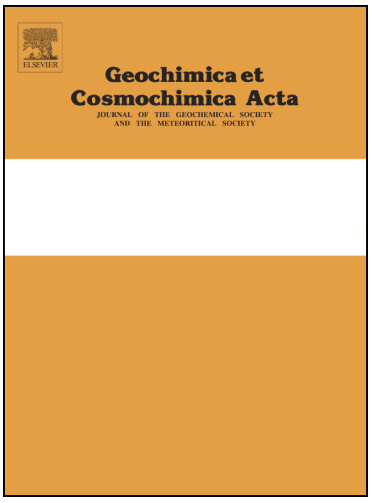

Mechanisms and rates of pyrite formation from hydrothermal fluid revealed by iron isotopes

Gleb S. Pokrovski, Marc Blanchard, Gaëlle Saunier, Franck Poitrasson

PII: S0016-7037(21)00152-6
DOI: https://doi.org/10.1016/j.gca.2021.03.006
Reference: GCA 12120

To appear in: *Geochimica et Cosmochimica Acta*

Received Date: 4 November 2020
Revised Date: 28 February 2021
Accepted Date: 4 March 2021

Please cite this article as: Pokrovski, G.S., Blanchard, M., Saunier, G., Poitrasson, F., Mechanisms and rates of pyrite formation from hydrothermal fluid revealed by iron isotopes, *Geochimica et Cosmochimica Acta* (2021), doi: https://doi.org/10.1016/j.gca.2021.03.006

Mechanisms and rates of pyrite formation from hydrothermal fluid revealed by iron isotopes

Gleb S. Pokrovski*, Marc Blanchard, Gaëlle Saunier, Franck Poitrasson

Géosciences-Environnement-Toulouse (GET), UMR 5563 du CNRS, Université Paul Sabatier Toulouse III, IRD, CNES, OMP, 14, avenue Edouard Belin, F-31400 Toulouse, France

* Corresponding author

e-mail: gleb.pokrovski@get.omp.eu; Phone: +33 (0)5 61 33 26 18; Fax: +33 (0)5 61 33 25 60

Geochimica et Cosmochimica Acta

ms # GCA-D-20-01014

Revision 1

28 February 2021

ABSTRACT

Critical to interpreting iron isotope signatures in hydrothermal sulfide minerals is the accurate knowledge of Fe isotope fractionation factors, both kinetic and at equilibrium, between the fluid and minerals. Here we report Fe isotope fractionation between pyrite and aqueous saline fluid from in-situ pyrite precipitation experiments performed at 400–450°C and 400–800 bar in a wide range of pH (2.5–4.8) and salt content (0.05–2.0 mol NaCl/KCl per kg of fluid). Our measurements show that while apparent bulk chemical equilibrium (in terms of total dissolved Fe concentration) between the $FeCl_2$-bearing fluid and crystalline pyrite is attained within a few days, the Fe isotope fractionation values between the fluid and mineral (expressed as $\Delta^{57}Fe_{fluid\text{-}pyrite} = \delta^{57}Fe_{fluid} - \delta^{57}Fe_{pyrite}$) exhibit large variations, from about –0.6 to +1.0‰, depending on the elapsed time (1–30 days) and fluid composition (mostly pH, sulfur solubility, and di- and tri-sulfur radical ion concentration). Yet these values remain significantly higher, by 0.5–2‰, than equilibrium isotope fractionation inferred from β-factors of pyrite and the dominant iron chloride species in solution $FeCl_2(H_2O)_2^0(aq)$, generated in this study using Density Functional Theory (DFT) modeling ($\Delta^{57}Fe_{FeCl_2(H_2O)_2\text{-}pyrite} \approx -1.25\pm0.25$‰ at 300–450°C). The lack of isotope equilibrium between fluid and pyrite in this study and other recent work demonstrates that the fluid-pyrite Fe isotope exchange is kinetically controlled even at elevated temperatures (≥300°C), allowing rate patterns to be identified. Our time-series data, combined with other available measurements at 300–350°C, provide evidence for two major distinct kinetic regimes of fluid-pyrite Fe isotope exchange: 1) a fast and short (<10–20 days) initial step, likely controlled by Fe (poly)sulfide aqueous precursors that transfer their isotope signature to rapidly precipitating pyrite resulting in apparent isotopic disequilibrium between the $FeCl_2$-dominated fluid and pyrite, 2) followed by a slower and longer second step of pyrite recrystallization, growth, and isotope re-equilibration with the fluid. The derived Fe isotope exchange rate constants suggest that more than 1 year is required to isotopically equilibrate pyrite with hydrothermal fluid at temperatures of 300–450°C. Our new data provide direct interpretation of the Fe isotope ratios in fluids and sulfide minerals from modern submarine hydrothermal vents, which are characterized by fast (hours to days) pyrite precipitation. Furthermore, our results may enable estimating, using Fe isotope signatures, the dynamics of relatively short (<year-scale) mineralizing events in ancient hydrothermal metal sulfide deposits that cannot be assessed using more traditional approaches.

Key-words: Iron isotopes; hydrothermal fluid; pyrite; Fe aqueous speciation; Fe (poly)sulfide complexes; isotope exchange rate; β-factor, magnetic spin

Highlights:

- Our experiments simulate in-situ pyrite precipitation from hydrothermal fluids at 400-450°C
- Theoretical β-factors of minerals and aqueous species constrain equilibrium isotope fractionation
- Aqueous Fe(II)-(poly)sulfide species control pyrite nucleation and isotope signatures
- A two-step kinetic model accounts for Fe isotope exchange between fluid and pyrite
- Rate constants enable estimations of dynamics of short-term (~years) mineralizing events

1. Introduction

Iron isotope ratios in sulfide minerals provide a powerful tool for tracing hydrothermal processes (e.g., Graham et al., 2004; Rouxel et al., 2003, 2004, 2008; Wawryk and Foden, 2015; Syverson et al., 2013, 2017). For example, pyrite from mid-ocean ridge (MOR) hydrothermal vents from Atlantic and Pacific oceans, that typically forms at temperatures of 200–400°C, exhibits large variations in δ^{57}Fe values (see section 2.2 for notations), from –4.5‰ to +0.8‰, depending on the locality (Rouxel et al., 2003, 2008; Syverson et al., 2017 and references therein). On the continents, pyrite and chalcopyrite from the Grasberg Cu–Au deposit (Indonesia), for example, have a δ^{57}Fe value range of –3.0 to +1.6‰ (Graham et al., 2004). Subsequent work on different continental magmatic-hydrothermal and metamorphic Fe-Cu-Au-Sn-W sulfide ore deposits confirmed notable Fe isotope variations in pyrite over a range of at least ~2‰, whereas other major Fe-bearing minerals such as chalcopyrite, pyrrhotite or magnetite usually exhibit smaller variations of δ^{57}Fe values (Markl et al., 2006; Wang et al., 2011; Cheng et al., 2015; Pi et al., 2015; Wawryk and Foden, 2015; Li et al., 2018; Zhu et al., 2018). Likewise, direct data for dissolved iron isotope compositions in modern hydrothermal fluids from MOR show variations of δ^{57}Fe values over at least 1.5‰ (e.g., Sharma et al., 2001; Beard et al., 2003; Rouxel et al., 2008; Bennett et al., 2009; Syverson et al., 2017).

These significant Fe isotope fractionations in hydrothermal-magmatic (and also sedimentary) environments may reflect a variety of factors related to the source of rocks and fluids, temperature (*T*), pressure (*P*), redox conditions, fluid chemistry, iron and sulfur aqueous speciation, kinetics of mineral precipitation and growth, and dynamics of hydrothermal activity. For example, δ^{57}Fe-depleted pyrite signatures from MOR vents were hypothesized to reflect out-of-equilibrium fractionation due to the initial formation of FeS precursors (e.g., Rouxel et al., 2008; Syverson et al., 2013), whereas δ^{57}Fe-enriched pyrite signatures from some ancient ore deposits might reflect equilibrium isotope fractionation (e.g., Wang et al., 2011; Wawryk and Foden, 2015). The isotopic composition of the source fluid could also contribute to the δ^{57}Fe signatures in sulfide minerals from some continental ore deposit settings (Markl et al., 2006). However, to enable predictive models, a quantitative assessment of these complex fractionation patterns depending on the geological context yet awaits more accurate knowledge of both equilibrium and kinetic Fe isotope fractionation factors coupled with a better understanding of molecular-level chemical speciation in mineral-fluid systems at elevated *T*-*P*.

Theoretical quantum-chemical calculations and spectroscopic techniques (Mössbauer and nuclear resonance inelastic X-ray scattering, NRIXS) have provided values of β-factors (see section 2.4 for notations) for major Fe-bearing minerals such as pyrite, hematite, magnetite, chalcopyrite and troilite (e.g., Polyakov et al., 2007, 2019; Blanchard et al., 2009; Rustad and Dixon, 2009; Polyakov and Soultanov, 2011). Progress in molecular modeling has also motivated numerous theoretical calculations of β-factors for some Fe(II) and Fe(III) aqueous species, including the Fe^{2+} and Fe^{3+} cations and few chloride

complexes (Schauble et al., 2001; Anbar et al., 2005; Domagal-Goldman and Kubicki, 2008; Hill and Schauble, 2008; Hill et al., 2010; Rustad et al., 2010; Fuji et al., 2014). However, these data exhibit variations up to several ‰ in β-factor values for the same species according to different studies and chosen computational approaches and, more importantly, these data lead to fluid-mineral fractionations that sometimes vary significantly (e.g., Saunier et al., 2011; Dauphas et al., 2017 for an overview). Moreover, we note a lack of data for many other Fe species, including various (poly)sulfide and chloride complexes, that likely form in Cl-S-rich hydrothermal fluids. Therefore, experimental calibrations of fluid-mineral Fe isotope exchange reactions over a wide *T-P* range of hydrothermal conditions are necessary both for interpreting the natural data and better reconciling the theoretical models.

Yet, experimental data of iron isotope fractionation in fluid-mineral systems remain rare at T >100°C (Saunier et al., 2011; Syverson et al., 2013, 2017), compared to lower-T data (<100°C), which focused on various Fe oxide/hydroxide/carbonate/sulfide - fluid systems (e.g., Skulan et al., 2002; Wiesli et al., 2004; Butler et al., 2005; Beard et al., 2010). In these low-T experiments, attainment of isotope equilibrium is very slow and kinetic fractionation is dominant. For example, Butler et al. (2005) and Guilbaud et al. (2010) measured the Fe isotope fractionation between aqueous solution (with the Fe^{2+} cation as the major Fe species) and synthetic mackinawite (FeS, mack), and showed a significant kinetic effect, with $\Delta^{57}Fe_{fluid\text{-}mack}$ values decreasing from ~1.3‰ at the start of mackinawite precipitation to ~0.5‰ after several weeks of reaction. Subsequently, Guilbaud et al. (2011) and Wu et al. (2012) pursued such experiments and agreed on the equilibrium $\Delta^{57}Fe_{fluid\text{-}mack}$ fractionation factor being about –0.5‰ at near-ambient neutral pH conditions, whereas mackinawite synthesis at acidic pH was affected by strong kinetic controls due to faster agglomeration of FeS particles. In addition, Wu et al. (2012) provided compelling evidence for an effect of Fe-sulfide aqueous complexes on mackinawite-fluid Fe isotope fractionation.

Although these experiments call upon the importance of iron aqueous speciation for Fe isotope fractionation during sulfide mineral (FeS) formation, they do not allow, however, straightforward interpretations of Fe isotope fractionations in natural hydrothermal systems. This is because of the different Fe aqueous speciation in high *T-P* saline fluids, dominated by Fe-chloride complexes, variable S speciation including in addition to H_2S other S redox forms (sulfate, polysulfides, sulfur dioxide and molecular sulfur, e.g., Kokh et al., 2020), and the ubiquity of pyrite. A pioneering advance in closing the gap between nature and laboratory has been made by Syverson et al. (2013) who conducted pyrite precipitation experiments at 300 and 350°C in S-bearing acidic saline fluids and found that even at such high temperatures, kinetic effects still control Fe isotope exchange between aqueous fluid and pyrite, leading to a depletion of the initially forming solid in ^{57}Fe isotope relative to the fluid. Pushing further by using the partial isotope exchange technique, Syverson et al. (2013) could elegantly determine the fluid-pyrite Fe isotope equilibrium with a fractionation factor $\Delta^{57}Fe_{fluid\text{-}pyite}$ of –1.5±0.4‰ at 350°C and 500 bar, which is in reasonable agreement with available theoretical predictions of β-factors for pyrite and the Fe^{2+} cation (Blanchard et al., 2009; Rustad and Dixon, 2009; Rustad et al., 2010). However, Fe aqueous speciation in

hydrothermal fluids is dominated by species other than Fe^{2+} whose abundance depends on salinity, S content and speciation, and pH (e.g., Saunier et al., 2011). As a result, the rates of fluid-mineral isotope exchange, as well as controlling molecular mechanisms and precursors of pyrite precipitation remain insufficiently understood to allow accurate interpretation of the rapidly growing body of Fe isotope measurements on natural pyrite and other Fe-bearing minerals both in active hydrothermal systems and ancient mineral deposits.

To further explore the molecular mechanisms and rates governing pyrite precipitation and fluid-mineral Fe isotope exchange over a larger range of temperatures and fluid chemistry, we conducted a series of precipitation experiments in the system pyrite-aqueous saline fluid across a wide range of salinity (0.05–2.0 m NaCl and/or KCl, where m is molinity, i.e. the number of moles of solute per 1 kg of fluid) at 400–450°C and 400–800 bar, pertinent to the conditions of many hydrothermal-magmatic metal deposits on Earth. The experimental data were combined with quantum chemistry calculations of β-factors of different aqueous Fe chloride and sulfide species and sulfide minerals, insufficiently covered by earlier studies. Put together, our results confirm previous work by demonstrating that disequilibrium Fe isotope fractionation effects for pyrite are ubiquitous across a wide range of temperatures and fluid compositions, even in situations where fluid-mineral chemical equilibrium is rapidly reached. Our data enable a deeper and quantitative insight into iron isotope exchange rates and pyrite formation mechanisms in hydrothermal systems and, therefore, help the interpretation of Fe isotope data obtained on pyrite-bearing samples in nature.

2. Materials and methods

2.1. Summary of experimental and analytical techniques

Hydrothermal experiments of in-situ pyrite precipitation were conducted at 400 and 450°C and between ~400 and ~800 bar in aqueous solutions NaCl-KCl-S-$FeSO_4$/$FeCl_2$ (±silicate minerals) of previously determined Fe isotope composition. The chemical composition of the experimental systems and the major fluid parameters at each experimental step are summarized in Table 1. These parameters have been chosen *i)* to enable high enough Fe concentrations in solution to be accurately processed and analyzed by MC-ICPMS, *ii*) to avoid the formation of mineral phases other than pyrite, *iii*) to produce comparable Fe pools between solid and solution for a more efficient chemical and isotope exchange and a more accurate derivation of δ^{57}Fe values for the precipitated pyrite and the coexisting fluid, and *iv*) to enable both pH and redox buffering to better constrain Fe aqueous speciation and pyrite solubility which is strongly dependent on these parameters.

The experimental strategy consists in the following steps: *i*) pre-equilibrating an aqueous sulfur-bearing solution at the given *T-P*, *ii*) injecting an $FeCl_2$ or $FeSO_4$ aqueous solution to induce pyrite precipitation while leaving significant concentrations of aqueous Fe in the fluid (100–1000 ppm), *iii*)

periodically sampling the fluid for chemical and Fe isotope analyses, and *iv*) recovering the precipitated pyrite for Fe isotope analyses at the end of the experiment (Fig. 1).

The initial sulfide-rich solution was generated by dissolving a given amount of native sulfur (S^0) at the run *T* in a salt-bearing aqueous fluid whose pH was either buffered by alkali aluminosilicate assemblages (runs m14 and m18) or by sulfur dissolution itself (runs m15 and m20). The use of S^0 as the starting material enables in-situ generation at elevated *T-P* of sufficient H_2S concentrations necessary for pyrite formation, as well as redox and pH buffering through the hydrogen sulfide - (hydrogen) sulfate equilibria (e.g., Pokrovski et al., 2009, 2015), yielding acidic pH (2–4) and oxygen fugacity in the vicinity of the conventional hematite-magnetite mineral buffer (HM), according to the reactions:

$$4\ S^0 + 4\ H_2O = 3\ H_2S + HSO_4^- + H^+ \quad (1)$$

$$HSO_4^- = SO_4^{2-} + H^+ \quad (2)$$

$$H_2S + 2\ O_2 = HSO_4^- + H^+ \quad (3)$$

Along with the dominant sulfate and sulfide species formed by those reactions, other species such as SO_2, sulfate ion pairs with K^+ and Na^+, and the di- and tri-sulfur radical ions $S_2^{\bullet-}$ and $S_3^{\bullet-}$ contribute to S aqueous speciation depending on *T*, pH and composition. Their concentrations may accurately be predicted using thermodynamic modeling (Table 1). The acidic pH chosen for this type of experiments *i)* allow enhanced pyrite solubility and, therefore, sufficient aqueous Fe in solution for accurate analytical and isotopic measurements; *ii)* favor rapid equilibration among different aqueous sulfur redox forms (e.g., Ohmoto and Lasaga, 1982; Kokh et al., 2020); and *iii)* enable direct comparisons with similar studies in hydrothermal solution conducted at acidic pH (e.g., Syverson et al., 2013).

Alternatively, the fluid pH was buffered by the K^+/H^+ equilibrium via the reactions between the fluid and silicate minerals:

$$1.5\ \text{microcline} + H^+ = 0.5\ \text{muscovite} + 3\ \text{quartz} + K^+ \quad \text{(QMM buffer)} \quad (4)$$

$$\text{muscovite} + H^+ = 1.5\ \text{andalusite} + 1.5\ \text{quartz} + 0.5\ H_2O + K^+ \quad \text{(QMA buffer)} \quad (5)$$

Such experiments provide less acidic pH (4–5, at our *T-P*-salinity parameters) than those with S^0 alone, more relevant to those of hydrothermal-magmatic fluids associated with granitic and andesitic rocks, but they require at least several days to fully equilibrate at our laboratory conditions. Overall, the experimental conditions chosen in this study are fully pertinent to porphyry Cu-Au-Mo and associated epithermal systems in volcanic arc settings, characterized by a large range of salinities (to ~20 wt% NaCl equivalent), acidic pH (i.e. sericite alteration), the presence of hematite, magnetite, and alunite along with pyrite and Cu sulfide minerals, and the coexistence of sulfate and sulfide in the fluid phase (e.g., Eunaudi et al., 2003; Kouzmanov and Pokrovski, 2012; references therein).

Our experimental methodology, by using pre-equilibrated S-bearing solutions before reacting them with Fe(II), differs from that employed by Syverson et al. (2013) who used thiosulfate as the source of sulfur injected into acidic Fe(II) solution to precipitate pyrite. Thiosulfate decomposition to sulfate and

sulfide is a relatively slow multi-stage process (e.g., Kokh et al., 2020) that might complicate the interpretation. Despite these differences, both our and Syverson et al.'s (2013) study yielded very similar Fe isotope fractionation patterns (see below), confirming the validity of both approaches and, more importantly, the universality of the reaction mechanisms.

All experiments also contained Au and Pt as metallic pieces, and two experiments (m14 and m18) had in addition ~100s ppm of Zn(II) and Cu(I) in the form of chloride salts. Inclusion of these components in the experiments permits to approach more closely the composition of natural hydrothermal fluids and to check for the effect of those metals on Fe isotope fractionation. Furthermore, in the final stage of one experiment at 450°C (m18), the pressure was decreased to ~400 bar to un-mix the initial supercritical fluid into vapor and brine, and to directly measure Fe isotope fractionation between the two phases to better account for the effect of fluid immiscibility phenomena common in hydrothermal-magmatic systems (Pokrovski et al., 2008; Kouzmanov and Pokrovski, 2012).

The experiments were performed in a rocking hydrothermal reactor Coretest equipped with a titanium flexible cell (Seyfried et al., 1987; Pokrovski et al., 2008). Rocking was important for such kind of experiments with large fluid volumes (100 mL) both to reduce temperature gradients in the cell and to well mix the reactants, thereby avoiding concentration gradients and associated diffusion issues that may strongly affect mineral nucleation and out-of-equilibrium crystal growth. To precipitate pyrite, injections of freshly prepared degassed $FeCl_2$ or $FeSO_4$ solutions were achieved with a manual volume-calibrated pump. Before and after pyrite precipitation, small amounts of solution (~2 g) were periodically extracted via high *T-P* titanium tubing and valves and trapped into a titanium vial, as described in detail by Kokh et al. (2017, 2020). The rapid fluid transfer into the vial (<1 s) under experimental pressure avoids solute loss through metal sulfide precipitation and volatile sulfur degassing during sampling of S-rich fluids at elevated temperatures. The sampled solutions were processed and analyzed using established protocols (Pokrovski et al., 2008; Saunier et al., 2011; Kokh et al., 2016, 2017). Briefly, Fe, Na, K, Zn, Cu, Si, Au and Pt concentrations were determined by inductively coupled plasma - mass spectrometry (ICP-MS) and, selectively, by flame atomic absorption spectrometry (FAAS) and by inductively coupled plasma - atomic emission spectrometry (ICP-AES). Reduced sulfur (S_{red}, including H_2S, and eventually SO_2 and polysulfide ions) was quantified by iodometric titration. In selected samples, hydrogen sulfide (H_2S) was separated from the other sulfur forms by adding in the sample vial Cd acetate inducing precipitation of CdS, followed by its centrifugation and iodometric titration. Total dissolved sulfur (S_{tot}) was analyzed as the SO_4^{2-} anion, together with the Cl^- anion, by high performance liquid chromatography (HPLC) after total oxidation of sulfur by H_2O_2 in aqueous NH_3 solution. The analytical data together with their uncertainties are reported in Appendix B (Table B.1). The redox-sensitive dissolved metals were present in the fluid in their oxidation states occurring in natural hydrothermal systems (i.e. Fe(II), Zn(II), Cu(I), Au(I), Pt(II)) as inferred from *i)* visual observation of sampled fluids, which were slightly green as typical for the Fe^{2+} cation, *ii*) analyses of the solids recovered after experiments, which did not show any evidence for Cu(II)- or Fe(III)-bearing phases, and *iii)* thermodynamic calculations using available data for aqueous metal complexes and mineral

phases (see section 2.3). The solids recovered after experiments were analyzed by X-ray diffraction (XRD), scanning electron microscopy (SEM) and electron probe micro-analyzer (EPMA). They showed pyrite as the only Fe-bearing phase in all experiments (Fig. 2). Silicate minerals (in m14 and m18) showed no detectable phase or compositional changes after the experiments.

2.2. Iron isotope analyses

Iron isotope compositions measured or discussed in this study are conventionally expressed in the delta notation as $\delta^{57}Fe$ relative to the average ratio of IRMM-014 metallic iron reference material:

$$\delta^{57}Fe \text{ (in ‰)} = [(^{57}Fe/^{54}Fe)_{sample}/(^{57}Fe/^{54}Fe)_{IRMM\text{-}014} - 1]\times 1000 \quad (6)$$

In cases where the ^{56}Fe isotope was reported in the original data sources, its δ-values were converted to the ^{57}Fe scale using the mass-dependent relationship: $\delta^{57}Fe \approx 1.50 \times \delta^{56}Fe$. The fractionation factor between an aqueous Fe species or bulk hydrothermal fluid (A) and an Fe-bearing mineral (B) is expressed as the difference of their respective $\delta^{57}Fe$ values:

$$\Delta^{57}Fe_{A\text{-}B} = \delta^{57}Fe_A - \delta^{57}Fe_B \quad (7)$$

Two milliliters of sampled solution were evaporated to dryness at 120°C on a hotplate, followed by reaction with 2–3 mL of aqua regia (9 M HCl + 15 M HNO_3 in 1:2 volume ratio, were M is molarity, mol/L) at 120°C during 24 h, and again evaporated to dryness. Three to five mL of 6 M HCl were then added to the residue and digested at 120°C for 24 h, and then again evaporated to dryness. The final precipitate was dissolved in 5–7 mL of 6 M HCl (depending on Fe concentration). Half mL of this solution was loaded into thermo-retractable Teflon columns and purified twice using the anionic resin BioRad AG1 X4 (200–400 mesh), following the procedure in Poitrasson et al. (2004). The processed solution was evaporated and then diluted to 50–100 ppm Fe by addition of 0.05 M HCl and stored for iron isotope analyses. This solution was further diluted to 2–4 ppm Fe in 0.05 M HCl (depending on the instrument sensitivity) just before an analytical session.

Iron isotope ratios were measured using a Thermo Electron Neptune magnetic sector - inductively coupled plasma - mass spectrometry (MC-ICP-MS) at GET (Toulouse), after the addition of Ni for internal mass-bias correction. The detailed protocol may be found in Poitrasson and Freydier (2005). Each sample was measured 6 times. The IRMM-014 standard was placed before and after each sample in the analytical sequence. The long-term Fe isotope measurement reproducibility of our in-house Milhas hematite standard (Poitrasson and Freydier, 2005) for $\delta^{57}Fe$ values is ~0.013‰/amu (2SD). Values of $\delta^{57}Fe$ have been always ~1.50 times those of $\delta^{56}Fe$, demonstrating a mass-dependent relationship known for all terrestrial samples (Poitrasson and Freydier, 2005). Consequently, only the $\delta^{57}Fe$ values are reported here. Uncertainties on the $\delta^{57}Fe$ and $\Delta^{57}Fe$ values are expressed as two-standard error (2SE) as calculated from the number of replicates and using the Student's correction factor (Platzner, 1997).

2.3. Chemical equilibrium calculations of iron and sulfur speciation and solubility

Iron and sulfur chemical speciation and solubility in experimental solutions at equilibrium were modeled using available thermodynamic data and the results were compared with the measured concentrations. Calculations were performed using the HCh software based on the minimization of the Gibbs free energy of the system (Shvarov, 2008, 2015). To account for non-ideality of the saline fluid, activity coefficients of charged species were calculated using the extended Debye-Hückel equation, whereas those of uncharged species were set to be equal to one (Pokrovski et al., 2009). Thermodynamic properties of silicate minerals used for pH buffering and those of pyrite and other Fe sulfide and oxide minerals that might potentially form were adopted from the USGS database (Robie and Hemingway, 1995), and those of elemental sulfur (both solid and liquid) from the JANAF database (Chase et al., 1998). The thermodynamic properties of the major fluid constituents (H_2O, H^+, OH^-, Na^+, Cl^-, $NaCl^0$, HCl^0), traditional aqueous sulfur anions (HS^-, SO_4^{2-}, HSO_4^-, HSO_3^-, SO_3^{2-}, $S_2O_3^{2-}$, S_n^{2-}) and their ion pairs with Na^+ and K^+ were adopted from the SUPCRT 2007 database (Johnson et al., 1992), based on the revised and extended HKF equation of state (Oelkers et al., 2009; Sverjensky et al., 2014), and complemented by more recent data, including those for $S_2^{\bullet-}$ and $S_3^{\bullet-}$ (see for details and references Pokrovski et Dubessy, 2015; Pokrovski et al., 2019; Kokh et al., 2020). The thermodynamic properties of aqueous H_2S and SO_2 were taken from Akinfiev and Diamond (2003) whose model yields a more accurate description than the HKF model over the *T-P* range relevant to our study, yet being consistent with their anionic counterparts from the SUPCRT database. The calculated pH, redox, sulfur saturation index (SI), and major S species concentrations at the *T-P* conditions of each experiment are reported in Table 1.

The thermodynamic properties of aqueous Fe^{2+} and its hydroxide complexes were adopted from Shock et al. (1997) whereas those of Fe(II) chloride species, $FeCl^+$ and $FeCl_2^0$, were taken from Sverjensky et al. (1997), which are in agreement with most available solubility and UV-spectroscopy data in a wide *T-P* range (to 600°C and 1 kbar) published over more than 5 decades (Wood and Samson, 1998; Saunier et al., 2011; references therein). To this largely adopted set of data for Fe(II) chloride complexes, an additional higher-order chloride complex, $FeCl_4^{2-}$, was added for evaluation. Its stability constants stem from the X-ray absorption spectroscopy (XAS) study of Testemale et al. (2009) who suggested the dominant formation of $FeCl_4^{2-}$ over wide *T* and chloride concentration ranges (>0.1 m Cl at 400−450°C and 500 bar). However, inclusion of this species in the calculations yielded either a negligible contribution to pyrite solubility in low-salinity fluids of this study (<1 ppm Fe at 0.05 m Cl, in runs m15 and m20) or unrealistically high solubility in highly saline fluids (>1000s to 10,000 ppm Fe at 2 m Cl, in runs m14 and m18). In the light of these discrepancies with the measured values, the too limited available dataset for $FeCl_4^{2-}$, and the uncertainties associated with its unambiguous identification from XAS spectra (see Testemale et al., 2009 for discussion), we have not considered further this species in the interpretation of the Fe isotope fractionation patterns in the present study. An alternative or additional higher-order Fe(II) chloride complex in saline fluids invoked in recent literature is $FeCl_3^-$ (e.g., Testemale et al., 2009;

Scholten et al., 2019), but the absence of report of its stability constant in those works prohibits the contribution of such species to be assessed in our experiments.

A possible contribution of the ferric iron, Fe(III), chloride species has also been checked by including the $FeCl_3^0$ complex whose stability constants were directly derived in Saunier et al. (2011) from hematite precipitation/dissolution experiments at *T-P*, salinities and pH similar to the present study. This species was found to be negligible (<0.1 ppb Fe) at S-bearing and more reduced conditions of the present study. An alternative dataset of stability constants of Fe(III) chloride species, including $FeCl_3^0$ and $FeCl_4^-$, was recently derived using UV-Vis spectrometry up to 200°C by Stefansson et al. (2019). We extrapolated their data to the *T-P* conditions of our study using either the density model (Stefansson et al., 2019) or the electrostatic Ryzhenko-Brysgalin model (Shvarov, 2015). The extrapolated data yielded unrealistic pyrite solubility, at least 10 to 100 times higher than that measured in all experiments of this study, and appear to be inconsistent with other direct data on Fe sulfide and oxide solubility (Wood and Samson, 1998). The large overestimation of Fe(III) concentrations is likely to be an artifact of extrapolations over too large a *T-P* range owing to fundamental limitations of such models for supercritical fluids. Therefore, given the dearth of available data on Fe(III) chloride species and large uncertainties of extrapolations to high *T-P*, such complexes were disregarded in the present study. In all experiments, calculations predict the di-chloride Fe(II) complex, $FeCl_2^0$, to be by far the dominant Fe species in the fluid, and pyrite to be the only Fe-bearing solid phase present. As will be shown below, Fe isotope fractionation data provide an independent confirmation of this speciation scheme.

2.4. Density Functional Theory (DFT) calculations of aqueous Fe species and minerals

Measured isotope fractionations between aqueous species and minerals can be compared with thermodynamic equilibrium fractionations, $\alpha_{A\text{-}B}$, between two phases (or species) A and B, determined from the reduced partition function ratios, also called β-factors, as:

$$1000\ln\alpha_{A\text{-}B} = 1000\ln\beta_A - 1000\ln\beta_B \approx \Delta^{57}Fe_{A\text{-}B} \text{ (in ‰)} \quad (8)$$

As thoroughly described by Blanchard et al. (2017), the β-factor can be determined by computing vibrational frequencies using a harmonic approach (Bigeleisen and Mayer, 1947):

$$\beta = \left[\prod_{i=1}^{3N} \prod_{\{q\}} \frac{\nu_{q,i}}{\nu'_{q,i}} \times \frac{exp\left(-h\nu_{q,i}/2kT\right)}{1-exp\left(-h\nu_{q,i}/kT\right)} \times \frac{1-exp\left(-h\nu'_{q,i}/kT\right)}{exp\left(-h\nu'_{q,i}/2kT\right)}\right]^{\frac{1}{nNq}} \quad (9)$$

where $\nu_{q,i}$ and $\nu'_{q,i}$ are the frequencies of the vibrational modes i = 1 to 3N along wavevector q for the two isotopologues (the prime symbol referring to the light isotope), N is the number of atoms in the crystal unit cell with n sites for the element of interest, T is the temperature in Kelvin, and h and k are the Planck and Boltzmann constants, respectively. The second product is performed on a sufficiently large grid of Nq q-points in the first Brillouin zone of crystals. This expression obeys the 'Redlich-Teller rule', which accounts for the fact that there should be no isotopic fractionation in the high-temperature limit. For

molecules (i.e. non-periodic compounds), the β-factor expression simplifies since the concept of wavevector *q* does not apply.

Values of β-factor of Fe isotopes for marcasite (FeS_2), mackinawite (FeS) and troilite (FeS) were determined following the same computational method as for pyrite (FeS_2) in Blanchard et al. (2009). This pyrite β-factor proved to be reliable by comparison with data derived from other techniques such as Mössbauer and NRIXS spectroscopies or isotope exchange experiments (Blanchard et al., 2012; Polyakov et al., 2013, 2019; Syverson et al., 2013). Vibrational frequencies were calculated from the optimized mineral structures using first-principles DFT-based methods as implemented in the Quantum ESPRESSO suite of codes that takes advantage of plane-waves and pseudopotentials (PWscf and PHonon codes; Giannozzi et al., 2009). Calculations used the Perdew-Burke-Ernzerhof (PBE) parametrized generalized gradient approximation (GGA) functional (Perdew et al., 1996). Ultrasoft pseudopotentials were taken from the PSlibrary 1.0.0 (Dal Corso, 2014). The wave-functions and the charge density were expanded in plane-waves with 100 and 800 Ry cutoffs, respectively. The *k*-point and *q*-point sampling was done using a regular grid in reciprocal space according to the Monkhorst and Pack (1976) scheme (Appendix A, Table A.1). With these computational parameters, the total energy is converged within 1 mRy/atom as well as the frequencies. Structural relaxations were made by optimizing both the atomic positions and the cell parameters. For mackinawite, the *c* lattice parameter was fixed to the experimental value (Lennie et al., 1995) in order to keep the cohesion of FeS_4 tetrahedral sheets stabilized by van der Waals forces. Calculations for mackinawite and troilite were spin-polarized, and an antiferromagnetic ordering was applied to troilite (Antonov et al., 2009) with magnetic moments free to relax.

For modelling iron aqueous species and calculating the vibrational frequencies of their isotopologues, we followed the same computational approach as Fujii et al. (2014) in order to extend their Fe β-factor database to other Fe chloride and sulfide species more pertinent to the hydrothermal conditions of this study. DFT calculations as implemented in the Gaussian 16 code (Frisch et al., 2016) were performed with the hybrid DFT B3LYP functional (Becke, 1993; Lee et al., 1988) on a selection of Fe(II) chloride and sulfide species. Electronic wave functions were described by the 6-311+G(d,p) basis set for all atoms. As shown by Fujii et al. (2014), the use of this basis set and not a lower one is required for accurate computing the β-factors of Fe aqueous species. An 'ultrafine' numerical integration grid was used, and the SCF (self-consistent field) convergence criterion was set to 10^{-9}. Only the first coordination sphere around the Fe atom was considered, without any forced symmetry. Adding explicitly additional solvation shells is probably necessary to obtain accurate absolute values for the β-factors (Rustad et al., 2010). However, a detailed investigation of this issue by Fujii et al. (2014) suggests that the relative fractionations between aqueous species described by the first coordination shell ($\Delta^{57}Fe_{A\text{-}B}$) are reliable enough to be comparable with experimental values. Furthermore, one must also keep in mind that building a second solvation shell on aqueous species displaying various ligands, in a consistent way and without introducing additional

uncertainties to the relative fractionations, would be a difficult task that is beyond the scope of the present study.

3. Results

3.1. Element concentrations, iron speciation, and pyrite solubility in the fluid phase

3.1.1. Concentrations of elements other than iron

Measured aqueous concentrations of each element (Fe, Na, K, Si, Zn, Cu, Au, Pt, S, Cl) and reduced sulfur (S_{red} and H_2S) are reported in Table B.1. In all experiments, Na, K and Cl behaved conservatively, being either constant before and after injection of the Fe solution (run m20), or displaying a slight decrease of concentrations upon the injection owing to the fluid dilution (runs m14 and m18), or showing an increase due to their introduction with the injected Fe solution (run m15). Dissolved silica concentrations are stable over the total duration of the experiments in the presence of silicate-quartz assemblages (m14 and m18) and correspond to quartz saturation at the corresponding *T-P* conditions. Gold solubility ranges from <1 ppm in most acidic runs (m15 and m20) to ~50 ppm in less acidic silicate-buffered experiments (m14 and m18), in good agreement with the known Au speciation (Pokrovski et al., 2015) dominated by $AuHS^0$ (acidic pH) and $Au(HS)_2^-$ plus $Au(HS)S_3^-$ (near-neutral pH). Dissolved Pt displays ppb-level solubility with no systematic trends. Base metals Cu and Zn (introduced in m14 and m18) do not show systematic trends upon pyrite precipitation. In two other experiments (m15 and m20), Cu and Zn were present in trace quantities (< few ppm) close to background levels of the flexible-cell reactor. Upon fluid unmixing due to decompression (m18), all metals show consistent partitioning between the two phases, with Na, K, Si, Zn and Cu being enriched in the brine phase compared to vapor, and Au displaying an opposite fractionation in favor of the vapor phase. These trends are in excellent agreement with the available data and models on metal vapor-liquid partitioning (e.g., Pokrovski et al., 2013 and references therein).

Total sulfur concentrations (S_{tot}) measured in the sampled fluids before the Fe-bearing solution injection in the experiments at 450°C (m14, m18, m20) exhibit some scatter, yet are close, on average, to the initially loaded contents, in agreement with the high S^0 solubility at this *T* (>1 m S) as predicted by thermodynamic modeling. In the experiment at 400°C (m15), the S_{tot} concentrations are lower (Table B.1) than those initially loaded, in agreement with the lower S^0 solubility (Table 1). The concentrations of S_{tot} in the S^0_{liquid}-undersaturated runs at 450°C drop after the Fe injection, reflecting pyrite precipitation. Concentrations of H_2S and S_{red} were also monitored in the sampled fluids (Table B.1) but showed systematically lower values than predicted by thermodynamics (Table 1). This discrepancy is owing to the very rapid recombination of sulfide and sulfate to S^0 (reverse of reaction 1) and re-equilibration of the cooling fluid with native sulfur during the sampling, as discussed in more detail in Appendix B. Thus,

accurate quantification of the different S species existing at high *T-P* in acidic S-rich fluids of this study would require in-situ measurements and cannot be achieved by sampling techniques, which are reliable for analyzing bulk element concentrations. Therefore, in the following interpretation of iron solubility, speciation and isotope fractionation we rather rely on the thermodynamically predicted sulfur speciation (Table 1).

3.1.2. Aqueous iron speciation and pyrite solubility

It can be seen in Fig. 3 that, following the injection of $FeCl_2$ or $FeSO_4$ solution, aqueous Fe concentrations dropped by a factor of ~2 (m14, m18) to 5–10 (m15, m20) due to pyrite formation, as measured in the first sample taken the day after the injection. The initial pyrite precipitation rates, expressed as $\log_{10}$(mol pyrite/kg fluid/day), vary over a narrow range, from –1.7 (m20) to –1.2 (m15), and are about 1 log unit lower than those from Syverson et al.'s (2013) experiments at 300 and 350°C. In the subsequent samples (>3 days) of the time series, Fe aqueous concentrations either remain constant (m14, m15, m18) or slightly decrease before attaining a steady state between ~10 and 30 days of reaction (m20). The attainment of an apparent steady state is slower than in the previous experiments, which showed bulk fluid-pyrite equilibration within <1 hour (Syverson et al., 2013). This difference is likely due to the use in our study of pH buffers (aluminosilicate minerals or native sulfur, reactions (1) to (5), section 2.1) that have a certain response time to the pH perturbation caused by injection of Fe-bearing solution and pyrite precipitation leading to pH acidification:

$$FeCl_2^0 + 2\ H_2S = FeS_2(\text{pyrite}) + H_2 + 2\ Cl^- + 2\ H^+ \quad (10)$$

The steady-state Fe concentrations (indicated by horizontal solid lines in Fig. 3) fall within the range of those predicted in equilibrium with pyrite using the stability constants of the $FeCl_2^0$ complex from Sverjensky et al.'s (1997) dataset and considering the uncertainties associated with those constants and with thermodynamic predictions of major fluid components (H_2S, Cl^-), redox and, in particular, pH - the parameter to which pyrite solubility is very sensitive (equation 10). These uncertainties are indicated by horizontal dotted lines delimiting maximum and minimum possible $FeCl_2^0$ concentrations. For comparison, calculations including $FeCl_4^{2-}$ from Testemale et al.'s (2009) study (shown by dashed grey lines in Fig. 3) either predict negligible concentrations of this complex in low-salinity fluids (m15, m20) or significantly overestimate the measured pyrite solubility in high-salinity runs (m14, m18). Thus, a revision of the thermodynamic properties of $FeCl_4^{2-}$ and other potential high-order chloride species (e.g., $FeCl_3^-$) would be required before these complexes could be used with confidence in speciation and solubility modeling across a wide *T-P*-salinity range.

3.1.3. Pyrite crystal habit

Scanning electron microscopy investigations of the solids recovered upon the run termination (Fig. 2) show pyrite to be the only Fe-bearing mineral phase. Other minor solid phases include solidified droplets of liquid sulfur (m15) and metallic gold particles (m14), precipitated upon fluid cooling. Pyrite crystals

display a large variability in grain size (from <1 μm to ~50 μm) and crystal habit (from cubic to octahedral to pentahedral). It is impossible to unambiguously identify different crystal generations and their relationships, given the too small set of microscopic data and possible modifications of originally precipitated pyrite during the long reactor cooling (hours). It is likely that the largest crystals would be the least affected by such modifications. Their dominant habit seems to correlate with the initial degree of Fe super-saturation expressed as the ratio between the initially injected aqueous Fe (Fe_0) and the steady-state measured Fe (Fe_{eq}) concentrations, $\Omega = [Fe]_0/[Fe]_{eq}$ (reported in Appendix C, Table C.2). Experiments with lower Ω values (2–4, m14 and m18) show predominantly pyritohedron-like habits (Fig. 3a,c,d), whereas those with higher Ω (32–34, m15 and m20) display mostly cubic and/or octahedral crystal shapes (Fig. 3b,e,f). This variability may in addition depend on many other parameters such as *T, P*, fluid composition, duration, degree of sulfur saturation, nature of precursors and the associated growth mechanisms (e.g., Murowchick and Barnes, 1987; Graham and Ohmoto, 1994). Even though their effects cannot be unambiguously identified in this study, they have a small impact on the apparent bulk chemical equilibrium that was rapidly attained (within its associated uncertainty margins) between the fluid and pyrite in our experiments over a wide range of initial parameters and fluid compositions (i.e. Ω(Fe), SI(S), pH, salinity, sulfur speciation, and pyrite precipitation rates; Tables 1 and C.2). This conclusion is in agreement with previous experiments of pyrite precipitation at lower temperatures and with different sulfur speciation (300–350°C, thiosulfate as sulfur source; Syverson et al., 2013), which showed even faster attainment of apparent chemical equilibrium, within <1 h, between a $FeCl_2$-dominated fluid and pyrite. Note that the precision of the solubility method to identify the attainment of true thermodynamic equilibrium is simply limited by the intrinsic precision of Fe dissolved concentration determinations, which are at best ±5% of the value (e.g., Table B.1). In contrast, Fe isotope ratios, which are ~1000 times more precise (±0.05‰), enable a far better 'resolution' of the fluid-mineral equilibration processes. Therefore, given accurate chemical constraints on the experimental system, the present results and previous work should warrant the interpretation of the Fe isotope data described below.

3.2. Experimental Fe isotope fractionation

In each experiment, Fe isotope compositions were analyzed in fluid samples, and those of pyrite were estimated in each sampling session from mass balance using the injected and sampled amounts of Fe (Table B.1) and Fe isotope ratios measured in the fluid (Table 2), as detailed in Appendix C. The isotope composition measured in pyrite recovered after the experiment was always in agreement, within errors, with the mass-balance calculated values (Table 2). The derived fluid and pyrite $\delta^{57}Fe$ values in each sampling session are shown as a function of time in Fig. 4. They are distinctly different from one another and from the initially injected Fe solution demonstrating a significant fluid-mineral Fe isotope fractionation. They show an evolution with time depending on the respective Fe amounts in the two phases.

For example, at advanced stages of experiments m18 and m20 (>10 days), the $\delta^{57}Fe_{pyrite}$ values are much less sensitive to time change than the $\delta^{57}Fe_{fluid}$ values, because pyrite represents ~90% of the total Fe reservoir in the system (Table 2). Using the $\delta^{57}Fe$ values measured in the fluid and calculated for pyrite, Fe isotope fractionation ($\Delta^{57}Fe_{fluid\text{-}pyrite}$) between fluid and pyrite is calculated as $\Delta^{57}Fe_{fluid\text{-}pyrite} = \delta^{57}Fe_{fluid} - \delta^{57}Fe_{pyrite}$, and displayed in Fig. 5 as a function of time elapsed from the moment of Fe injection in the reactor.

Three key observations can be drawn from these patterns. First, three experiments at 450°C (m14, m18 and m20) consistently display a rapid drop of the initially high $\Delta^{57}Fe$ values (~ +1‰) shortly after pyrite precipitation (<5 days), followed by an apparent steady state (for 5 to 15 days after injection) without systematic evolution of the $\Delta^{57}Fe_{fluid\text{-}pyrite}$ values, being between +0.5 and +0.7‰ (±0.2‰, on average among the data points at such apparent steady state, Table 2). Second, in the longest experiment (m20), a steady state (tentatively +0.45±0.15‰) is less clearly expressed between 5 and 20 days due to significant data scatter, yet $\Delta^{57}Fe$ values from two last samples (taken at 25 and 30 days) indicate a decrease to +0.2±0.1‰ (Fig. 5). This decrease would suggest that the steady state observed in the shorter-duration experiments (m14, m18) can only be apparent and much longer runs would be required to identify the temporal trends. Third, an exception to this pattern is experiment m15 at 400°C that yielded a negative $\Delta^{57}Fe_{fluid\text{-}pyrite}$ value from the start (–0.4±0.1‰; 1st sample taken 1 day after injection) being at least 1‰ lower than those in the other experiments and regularly decreasing with time over the run duration (7 days) without reaching a steady-state.

Remarkably, these patterns, as well as the absolute $\Delta^{57}Fe_{fluid\text{-}pyrite}$ values, appear to be very similar to the data reported by Syverson et al. (2013, 2017) from analogous experiments of pyrite precipitation at 300-350°C with faster attainment of equilibrium pyrite solubility (<1 h). To enable more direct comparisons with our results, we recalculated their data in terms of $\Delta^{57}Fe_{fluid\text{-}pyrite}$ at each sampling session using mass balance (Appendix C, Table C.1, Fig. 5b). It can be seen in Fig. 5b that, similar to our experiments (Fig. 5a), their positive $\Delta^{57}Fe_{fluid\text{-}pyrite}$ values (+0.5 to +1.5‰), measured shortly after pyrite formation for all four experiments conducted at 300 and 350°C, dropped by at least ~1‰ over 2 to 30 days of reaction, followed by pronounced flattening of this kinetic pattern vs time for longer-duration runs (350-2 and 350-3, up to 180 days). Even though the available dataset is yet limited, the strong similarity of chemical and isotope patterns in our and Syverson et al.'s work suggests some common mechanisms of pyrite formation and isotope exchange with the fluid. Their interpretation would require theoretical molecular-level knowledge of species structures and their isotope signatures as reported below.

3.3. Theoretical Fe isotope fractionation factors

To allow for a more systematic and robust comparison with the experimental data and identification of molecular-level controls on the observed Fe isotope fractionations, we have significantly extended the theoretical database of β-factors for Fe sulfide minerals and different Fe aqueous species pertinent to the context of this study.

As detailed in Appendix A, DFT-optimized lattice parameters of iron sulfide minerals are generally in good agreement with crystallographic values (i.e. within 0.6% in most cases). Theoretical vibrational frequencies also compare well with experimental values (within a few %). As a result, we assess that the derived mineral β-factors are assorted with a realistic relative uncertainty of about 5% of the value at the temperatures pertinent to hydrothermal contexts. The coefficients of polynomial fits of the generated β-factors and tabulated values at selected relevant temperatures are given in Table 3.

As shown in Fig. 6a, the predicted equilibrium fractionation between pyrite and aqueous $FeCl_2(H_2O)_2^0$ (see below calculations for aqueous species) is in excellent agreement with the experimental data of Syverson et al. (2013) obtained using the partial isotope exchange approach in long-term experiments at 350°C, thus providing support for the validity of our DFT method. We also compared, with the theoretical estimations, the experimentally measured isotope fractionation between mackinawite and aqueous Fe^{2+} at 2°C and 25°C by Guilbaud et al. (2011), and at 20°C and 35°C by Wu et al. (2012), which are in very good mutual agreement (Fig. 6b). The ^{57}Fe fractionation factors of Wu et al. (2012) between $FeHS^+$ or FeS^0 type of complexes and mackinawite measured in H_2S-rich solutions, which are 0.5‰ lower than with Fe^{2+}, are also comparable with the difference of the predicted β-factors between Fe^{2+} and $FeHS^+$ (Fujii et al., 2014), providing further support to their measurements. These available experiments indicate mackinawite to be slightly ^{57}Fe-enriched relative to aqueous Fe(II). This result would require a mackinawite β-factor significantly larger than that derived from Mössbauer data by Polyakov and Soultanov (2011), thus providing additional support to our calculations. The low-*T* experimental data would be consistent with a β-factor being in-between those of perfectly crystalline (i.e. ordered) and fully disordered mackinawite, as estimated in this study (Table A.3; Fig. 6b).

The optimized molecular structures and bond lengths of the investigated aqueous species are shown in Fig. A.3. In those complexes, Fe(II) has coordination numbers of 3, 4 or 6 with O, Cl or S as nearest atomic neighbors. In addition to the hexa-aquo Fe^{2+} cation, $Fe(H_2O)_6^{2+}$, a selection of 5 iron chloride complexes and of 7 iron (poly)sulfide complexes was modelled. These complexes were considered to be the most relevant species to the conditions and compositions of our experiments that are acidic (i.e., hydroxide species (OH^-) are less likely) and have Cl^-, H_2S (HS^-) and $S_3^{\bullet-}$ as the major potential ligands for Fe(II). Even though among these complexes $FeCl_2(H_2O)_2^0$ is likely to be dominant according to the thermodynamic analysis of our solubility data (section 3.1), other minor species undetectable by solubility or spectroscopic methods may also form and serve as reaction intermediates for pyrite precipitation. The corresponding β-factors and polynomial fits of their temperature dependence are reported in Fig. A.2 and Table 3. To enable us to provide an error estimation on our theoretical predictions, we tentatively apply to

aqueous species the same relative uncertainty of 5% as for minerals, which would correspond to absolute uncertainties of 1000lnβ values of <0.6‰ and <0.1‰ at 25°C and 450°C, respectively. Four out of those 13 species were already modeled by Fujii et al. (2014), namely $Fe(H_2O)_6^{2+}$, $FeCl(H_2O)_5^{+}$, $FeCl_2(H_2O)_4^{0}$ and $Fe(HS)_2(H_2O)_4^{0}$. Our optimized geometries and Fe β-factors are very similar to theirs, confirming that the DFT calculation software version (Gaussian 16 vs Gaussian 09) introduces no bias. Therefore, results for the new aqueous species investigated here can be considered as a consistent extension of the database produced by Fujii et al. (2014). In addition, Hill et al. (2010) investigated, both experimentally and theoretically, the redox and ligand effects on isotope fractionation in aqueous Fe-Cl solutions. It can be noted that the present β-factor values for $Fe(H_2O)_6^{2+}$, $FeCl(H_2O)_5^{+}$, and $FeCl_2(H_2O)_4^{0}$ fall within the small range of values that these authors found using the models UHF/6-31G(d) and B3LYP/6-31G(d). These models are the ones displaying the best agreement with experimental data of aqueous-ether fractionation for ferrous species in solutions of various chlorinity (e.g., see Fig. 6b of Hill et al., 2010). The present results thus confirm the little fractionation between the Fe(II) hexaquo cation and Fe(II) chloride species.

As shown in Fig. A.2 and Table 3, the two FeS_2 polymorphs (pyrite and marcasite) show very similar β-factors and the largest ones compared to the other solids. At the other end, troilite and disordered mackinawite show the lowest β-factors. The values of β-factors globally correlate with the average length of the bonds involving iron (Fig. 7) along two distinct trends. The 'lower' trend is composed of most aqueous species with Fe-O, Fe-Cl and Fe-S bonds that all follow the same trend. Species in which Fe have shorter bonds are ^{57}Fe-enriched at equilibrium compared to those having longer bonds, in agreement with the general isotope fractionation principles. Sulfide minerals seem to form a different ('upper') trend of β-factor versus bond length, even though the correlation is more scattered (Fig. 7) because other crystallochemical parameters are likely at stake. For example, Fe(II) can be either low-spin like in pyrite and marcasite or high-spin like in troilite and mackinawite. Iron can also be either in 4-fold coordination like in mackinawite or in 6-fold coordination like in the other minerals, and FeS_6 octahedrons share corners like in pyrite and marcasite, or edges and faces like in troilite (Fig. A.1). This variability of coordination geometries may contribute to generation of distinct trends for minerals and most aqueous species (Fig. 7). As described in section 2.4, the computational approach used for minerals and for aqueous species is different. The main difference lies in the functional used (e.g., PBE vs B3LYP). However, the functional alone does not explain the two trends observed in Fig. 7. For example, modelling the species $Fe(H_2O)_6^{2+}$ with the same functional as for the minerals (PBE) does not change much the results (i.e. with PBE functional, 1000lnβ = 1.49‰ at 400°C for a bond length of 2.155 Å, while 1000lnβ = 1.53‰ for a bond length of 2.165 Å with B3LYP functional; Table 3). On the other hand, we found that the electronic configuration of iron explains well the trends in Fig. 7. All aqueous species of the 'lower' trend have a high-spin configuration with 4 unpaired valence electrons, while the two low-spin species considered in this study ($Fe(HS)_2(S_3)_2(H_2O)_2^{2-}$ and $Fe(HS)_4(S_3)_2^{4-}$ where all Fe electrons are paired) fall on the 'mineral' trend. As a test, a virtual $Fe(H_2O)_6^{2+}$ species tentatively calculated in low-spin configuration would also

plot close to the mineral trend (i.e. 1000lnβ = 3.01‰ at 400°C for a bond length of 2.028 Å). These correlations may provide insight into molecular-level mechanisms of the formation of Fe sulfide minerals. Because Fe is in low-spin configuration in pyrite, its aqueous precursors, at some step of pyrite nucleation, would be expected to also be low-spin. These hypotheses warrant verification by experimental data as discussed in the following sections.

4. Discussion

4.1. Iron aqueous speciation and isotope fractionation in fluid-pyrite system

Our experiments, thermodynamic predictions, and the analysis of available literature data collectively demonstrate the dominant presence of the $FeCl_2^0$ complex in the aqueous fluid in equilibrium with pyrite. Note that the solubility data alone of a mineral in aqueous solution, being only sensitive to the electric charge and number of Cl^- ligands in the aqueous dominant complex (e.g., equation 10), cannot provide information about the exact complex geometry and the number of water molecules in the Fe coordination sphere that may impart isotope fractionation. Such information may only be gained from spectroscopic data or molecular modeling. The experimental $\Delta^{57}Fe_{fluid\text{-}pyrite}$ value may be directly compared with the theoretical equilibrium value of $1000ln\alpha_{species\text{-}pyrite}$, which is the difference of the corresponding β-factors of the species and the mineral derived in the previous section (equation 8). The β-factor for the species having $FeCl_2$ 'thermodynamic' stoichiometry corresponds to a 4-coordinated complex, $FeCl_2(H_2O)_2^0$, which is more stable at elevated *T* than 6-coordinated $[Fe(II)Cl_n(H_2O)_{6-n}]$ species prevalent in solution at ambient conditions, in agreement with direct spectroscopic (XAS, UV-Vis) data on metal chloride complexes (e.g., Fe, Co, Ni, Zn, Cd) that consistently show an octahedral-to-tetrahedral transition above ~200°C (e.g., Crerar et al., 1985; Bazarkina et al., 2010 and references therein). The theoretical $1000ln\alpha_{FeCl_2(H_2O)_2\text{-}pyrite}$ value is also in good agreement with the accurate isotope equilibrium measurements of Syverson et al. (2013) (Fig. 6). Therefore, this theoretical value will be used here as the reference for equilibrium fluid-pyrite Fe isotope fractionation over the investigated *T*-range.

It can be seen in Fig. 5a that the experimental steady-state $\Delta^{57}Fe_{fluid\text{-}pyrite}$ values for the three runs at 450°C (m14, m18 and m20) are at least ~1.5‰ higher than those predicted at equilibrium with pyrite. Such a difference can neither be explained by the uncertainties of theoretical β-factor values of pyrite and $FeCl_2(H_2O)_2^0$, which are ±0.1‰ at this temperature (see section 3.3), nor by a potential contribution from species like $FeCl_4^{2-}$ or $FeCl_3^-$ in saline fluids (m14, m18), because the β-factors for these species are all within only ~0.5‰ at 450°C (Table 3). In addition, the $\Delta^{57}Fe_{fluid\text{-}pyrite}$ values in the experiments that covered a large range of salinity (>15 wt% NaCl equivalent, e.g., m14 vs m20) do not show any consistent trends that could be connected with a putative Fe speciation change between the dominant $[FeCl_2]$ stoichiometry at low salinity to $[FeCl_{3\text{-}4}]$ at high salinity.

An independent support for $FeCl_2(H_2O)_2^0$ as the dominant aqueous species in saline fluids of our and previous (Syverson et al., 2013) experiments is provided by the direct measurement of Fe isotope fractionation between the vapor (~3 wt% NaCl+KCl) and brine (~16 wt% NaCl+KCl) phases in the last stage of experiment m18 (Tables B.1 and 2). The value of $\Delta^{57}Fe_{vapor\text{-}brine}$ is +0.12±0.10‰, demonstrating a close to zero Fe isotope fractionation between the two phases. The low-density and low-dielectric constant vapor phase has been shown to be dominated by electrically uncharged and thus more volatile species (Pokrovski et al., 2013 and references therein), which should be of $[FeCl_2]$ type. The absence of significant Fe isotope fractionation between vapor and brine strongly suggests that the same species should also be dominant in the saline liquid phase. If $FeCl_4^{2-}$ were dominant in the brine, the vapor-liquid fractionation should be close to +0.5‰ at 450°C according to the predicted β-factors (Table 3), which is significantly larger than the experimentally measured value (~0.1‰). Similar close-to-zero Fe isotope fractionations between vapor and brine were also reported by Syverson et al. (2014) at 420–470°C and liquid-phase salinities up to 30 wt%, indicating that $[FeCl_2]$ type of stoichiometry is likely to be the dominant in both phases.

In contrast to the three 450°C runs, the most acidic and S^0-saturated experiment at 400°C (m15) yielded $\Delta^{57}Fe_{fluid\text{-}pyrite}$ values of ~1‰ lower (≈ –0.5‰ on average), which regularly decreased over 7 days of run duration (Fig. 5) yet not reaching the theoretical equilibrium value with pyrite (–1.1±0.2‰). Again, this difference cannot be explained by potential variations in aqueous Fe dominant species ($FeCl_2^0$ vs higher-order chloride complexes) or pyrite supersaturation degree amongst the different experiments (e.g., experiment m20 of similar fluid composition and initial pyrite supersaturation degree yielded $\Delta^{57}Fe_{fluid\text{-}pyrite}$ values of 0.5 to 1.0‰ greater, Tables 2 and C.2). Consequently, the large and variable difference between theoretical equilibrium $\Delta^{57}Fe_{fluid\text{-}pyrite}$ values and those measured in this study is likely to be due to isotopic disequilibrium between pyrite and aqueous Fe whose amplitude and evolution may be controlled by the factors discussed below.

4.2. Kinetic isotope fractionation and solid-phase precursors during pyrite nucleation and growth

Kinetic factors related to faster diffusion and generally faster reaction rates of the light isotope during mineral nucleation and growth from aqueous solution might potentially contribute to the mineral enrichment by the light isotope compared to the equilibrium value (e.g., Hoefs, 2015; Watkins et al., 2017). Indeed, the first experimental samples in Fig. 5a,b display the highest $\Delta^{57}Fe_{fluid\text{-}pyrite}$ values meaning that the initially precipitated pyrite gets enriched in light isotopomers. However, such mechanisms alone are unlikely to be responsible for the Fe isotope disequilibrium patterns between the fluid and pyrite observed in the course of these and previous (Syverson et al., 2013) experiments. First, the amplitude of the ^{57}Fe fluid-pyrite disequilibrium, as may be quantified by the difference between the measured $\Delta^{57}Fe_{fluid\text{-}pyrite}$

values (Table 2) and the predicted equilibrium value at the corresponding temperature (Table 3, Fig. 6), does not show any significant correlation, across a wide temperature and compositional range, with either the initial degree of pyrite supersaturation or pyrite precipitation rate (Fig. C.2). Such correlations would have been expected in case of kinetic fractionation because those parameters are the main factors determining mineral precipitation and growth (e.g., Cole and Chakrabody, 2001; Watkins et al., 2017). Second, isotope fractionation that may be caused by faster diffusion of the light isotope of Fe(II) in the boundary layer of pyrite crystals growing in an aqueous medium is expected to be negligible, because the difference in diffusivities of Fe isotopes is rather weak in aqueous systems at near-ambient conditions (up to ~0.3‰; e.g., Rodushkin et al., 2004; Dauphas et al., 2017 and references therein), and is expected to be even smaller at elevated temperatures. We caution, however, that identification of kinetic effects at the very early stages, within the first hours, of pyrite nucleation at hydrothermal conditions in our and available studies currently lacks temporal resolution because of intrinsic difficulties of multiple sampling and analysis of high *T-P* experimental fluids within such short time frames. Investigation of these early stages of pyrite formation would ideally require in-situ time-resolved measurements or sophisticated flow-through high *T-P* setups which are not currently available. In the meantime, in the following analysis or our and previous experiments, we will treat as a single stage the Fe isotope disequilibrium between fluid and pyrite observed within an interval of several hours to several days after mixing of Fe- and S-bearing fluids.

An alternative (or complementary) interpretation of the ^{57}Fe-depleted (i.e. isotopically light) pyrite compared to aqueous solution observed in nature and experiments would be a mechanism of pyrite formation via a solid FeS-like precursor, resembling mackinawite or troilite. Such a mechanism has commonly been assumed to operate over a wide temperature range, from ambient up to at least 300°C (Schoonen and Barnes, 1991; Butler at al., 2005; Rouxel et al., 2008). This mechanism appears, however, unproven by the Fe isotope fractionation data at $T \geq 300$°C coupled with the theoretical calculations of fractionation factors. It can be seen in Fig. 5a,b that none of those solids considered as the pyrite precursor could consistently and systematically match the measured early $\Delta^{57}Fe_{fluid\text{-}pyrite}$ values in this study and previous work (Syverson et al., 2013). First, the theoretical equilibrium 1000lnα value between aqueous $FeCl_2(H_2O)_2^0$ and crystalline troilite and crystalline mackinawite calculated from their respective β-factors revised in this study are very different, the former being close to zero (+0.2‰) and the latter being far more negative and close to that of pyrite (–1.1 to –0.7‰ at 300–450°C, as can be computed from Table 3). Second, none of them matches the experimental $\Delta^{57}Fe_{fluid\text{-}pyrite}$ values at apparent steady state attained in certain runs or at the end of the runs without steady state (Fig. 5, with a possible single exception of m20). Third, the β-factor of highly disordered mackinawite appears to be very close to that of crystalline troilite, but ~1‰ lower than that for crystalline mackinawite. Even though such a wide range of possible β-factors for mackinawite of different degree of disorder might encompass the experimental $\Delta^{57}Fe_{fluid\text{-}pyrite}$ values in some of our and previous experiments, there is no any systematics between those values and the system composition, Fe concentration, degree of pyrite supersaturation or pyrite precipitation rate (e.g., Fig. C.2).

Thus, it is hard to imagine that mackinawite (or, by inference, troilite) of highly variable crystallinity and disorder degree would form in very similar experiments at similar conditions and would account for the large scatter of the measured values. Fourth, there is no significant correlation in the available dataset between $\Delta^{57}Fe_{fluid\text{-}mineral}$ values and the saturation index of FeS(troilite) S^0(liquid) (Fig. C.3), suggesting that such types of solid are unlikely to be universally involved in pyrite formation. Finally, we note that both mackinawite and troilite phases have Fe in high-spin configuration whereas Fe in pyrite is in low-spin. This difference would require significant (i.e. energetically expensive) electronic re-arrangements to form pyrite from such precursors. As a conclusion, none of the Fe sulfide phases considered here and in the literature as potential precursors of pyrite formation, would be consistent with the whole set of available hydrothermal experiments.

4.3. Aqueous Fe (poly)sulfide species as pyrite precursors

In the light of paucity of data to support evidence for simple kinetic isotope fractionation during pyrite nucleation and growth or FeS-like precursor phase formation in our and previous hydrothermal experiments, an alternative molecular-level approach to understand pyrite precipitation mechanisms at early stages would be to consider Fe aqueous species as possible direct precursors. Such (poly)sulfide-type polynuclear species [Fe_xS_y] might operate at early stages of pyrite precipitation before formation of larger colloid-like clusters or pyrite crystal nanoparticles as was commonly suggested for ZnS, FeS and FeS_2 mineral formation from aqueous solution at near-ambient conditions (e.g., Luther et al., 1999; Rickard et Luther, 2007 and references therein). At hydrothermal conditions, such bulky polymeric clusters are not expected to be stable due to increased thermal disorder and faster reaction rates at elevated temperatures favoring de-polymerization (e.g., Baes and Mesmer, 1976; Barnes, 1997). Mononuclear sulfide-type species, such as $FeHS^+$ and FeS^0, were also suggested to contribute to Fe isotope fractionation in near-ambient H_2S-rich solutions during FeS formation (Wu et al., 2012). Therefore, as a first approximation, a mononuclear type of species [$Fe(HS^-)_x(S_3^-)_y(H_2O)_z$], where $x+y+z = 4$ or 6, whose structures and β-factors were generated in this study (Table 3, Fig. A.3) may be considered as a reasonable proxy for molecular mechanisms of FeS_2 formation at elevated temperatures. Such species are expected to rapidly equilibrate, both chemically and isotopically, with the dominant aqueous $FeCl_2^0$ complex in the fluid, and to transmit their resulting Fe isotope signatures, without fractionation, to the rapidly precipitating pyrite.

To test this hypothesis, we compared the experimental $\Delta^{57}Fe_{fluid\text{-}pyrite}$ values from our and Syverson et al.'s (2013) study with the 1000lnα fractionation factors between the $FeCl_2(H_2O)_2^0$ complex dominant in the fluid and a given Fe-S species (i.e. difference of their respective β-factors). It can be seen in Fig. 5 that a number of possible Fe (poly)sulfide species in which Fe is generally 4-coordinated and in high-spin configuration (e.g., $Fe(HS)_2(H_2O)_2^0$, $Fe(HS)_4^{2-}$, $Fe(HS)_2(S_3)_2^{2-}$) may indeed account for the observed fluid-pyrite Fe isotope fractionation both in experiments at 450°C of this study and at 300–350°C in Syverson et

al.'s (2013) work, especially at early stages of fluid-pyrite isotope exchange reaction (<10 to 20 days). In contrast, for longer runs in Syverson et al. (2013) and for experiment m15 at 400°C in this study, the experimentally found fractionation ($\Delta^{57}Fe_{fluid\text{-}pyrite} \approx -0.5\pm0.5$‰, which is much closer to the equilibrium one (–1.25±0.25‰ on average, in the 300-450°C range) is better matched by species having 6-coordinated Fe in low-spin state (e.g., $Fe(HS)_2(S_3)_2(H_2O)_2^{2-}$, $Fe(HS)_4(S_3)_2^{4-}$). Remarkably, Fe in such type of species is similar, both structurally and electronically, to pyrite that has six-coordinated Fe in low-spin state (Fig. A.1). Such species likely develop at lower temperatures in more acidic and closer to S^0-saturated conditions (300–400°C, Fig. C.3) compared to the higher-temperature S^0-undersaturated systems (m14, 18 and 20 at 450°C). Therefore, depending on the fluid composition, the formation of either low-spin or high-spin and 6- or 4-coordinated aqueous Fe-(poly)sulfide precursors may adequately account for the large range of observed Fe isotope fractionations during pyrite formation. Interestingly, the experimental $\Delta^{57}Fe_{fluid\text{-}pyrite}$ values at the termination of the first kinetic stage of the experiments positively correlate with the thermodynamically predicted concentrations of radical ions and fluid pH (Fig. C.3). Indeed, these parameters should obviously control the resulting Fe (poly)sulfide species abundance. The presence of the $S_3^{\bullet-}$ ion, being a very reactive sulfur form itself due to an unpaired electron (Chivers and Elders, 2013), is further expected to favor rapid pyrite nucleation thus resulting in preferential enrichment of pyrite in light Fe isotopes, especially in solutions that have elevated radical ion concentrations (Fig. C.3). The exact identity and stability of the transient Fe (poly)sulfide species at a given temperature, fluid composition or acidity, is impossible to quantify solely by molecular modeling, and would require challenging in-situ spectroscopic approaches coupled with more systematic time-resolved Fe isotope data and space-resolved microanalyses of the growing pyrite crystals.

4.4. Mechanisms and rates of fluid-pyrite Fe isotope equilibration

The presently available experimental and theoretical dataset would be consistent with a two-stage mechanism with distinct kinetic patterns of Fe isotope equilibration between a saline hydrothermal fluid and pyrite (Fig. 8). The initial fast and short stage is controlled by transient (poly)sulfide aqueous species with Fe in low- or high-spin configuration that are in isotopic equilibrium with the dominant $FeCl_2(H_2O)_2^0$ complex in the fluid, characterized by a non-zero isotope fractionation factor $\Delta^{57}Fe$ between the chloride and sulfide species. These sulfide species may be either ^{57}Fe-depleted (in particular 4-coordinated and high-spin) or ^{57}Fe-enriched (e.g., 6-coordinated low-spin species) compared to $FeCl_2(H_2O)_2^0$, but all of them are generally ^{57}Fe-depleted relative to pyrite at equilibrium (Table 3). Upon fast pyrite nucleation, the mineral inherits those species isotope signature without fractionation, resulting in apparent isotope disequilibrium between the $FeCl_2$-dominated fluid and pyrite. This disequilibrium may attain as much as 1.5‰ in $\delta^{57}Fe$ between 300 and 450°C yielding $\delta^{57}Fe$-depleted pyrite. The degree of disequilibrium partly depends on the nature of the operating Fe-S aqueous precursor(s), which in turn may be function of various fluid

parameters (in particular pH and polysulfide ion abundance). This stage is followed by a slower and longer stage of pyrite isotope re-equilibration with the fluid. This second stage is required to describe the attainment of equilibrium and is expected to proceed by closer-to-equilibrium recrystallization and dissolution-precipitation processes with $\Delta^{57}Fe_{fluid\text{-}pyrite}$ values tending towards the true equilibrium one. Even though the available $\delta^{57}Fe$ kinetic dataset is rather limited, it is strongly suggestive of the second slower stage in the longest runs of Syverson et al. (2013) and this study (350-2, 350-3, m20; Fig. 5a,b).

Using the available time-series $\delta^{57}Fe$ data (Tables 2 and C.1), the rate constants of Fe isotope exchange between fluid and pyrite for the two kinetic stages may be derived following a simple first-order rate law (e.g., Johnson et al., 2002; Syverson et al., 2017):

$$\log_{10}(1-F) = -r_i \times t \quad (11)$$

where t is the elapsed time, r_i is the rate constant at each stage, and F is the extent of Fe isotope exchange relative to the equilibrium value:

$$F = (\Delta_0{}^{57}Fe - \Delta_t{}^{57}Fe) / (\Delta_0{}^{57}Fe - \Delta_{eq}{}^{57}Fe) \quad (12)$$

where subscripts 0, t and eq stand for Fe isotope fractionation between fluid and pyrite at time zero, at a given moment, and at equilibrium, respectively. For the first stage, Δ_0 was taken from the first sample after Fe injection in this and Syverson et al.'s (2013) study. For the second stage (when available), Δ_0 was approximated by the apparent steady-state value reached after the first step (m20, Table 2, Fig. 5a) or by the last sample taken before the $\Delta^{57}Fe$ kinetic pattern flattens (Table C.1 and Fig. 5b). The Δ_{eq} value for both steps was adopted as theoretical $1000\ln\alpha_{FeCl_2(H_2O)_2\text{-}pyrite}$ calculated at each given temperature. It can be seen in Table C.2 and Fig. C.1 that the derived r_1 values for the first step are remarkably similar and do not show any systematic trends (within reasonable uncertainties of 50%, as was roughly estimated from error bars on $\Delta^{57}Fe$ values) among available experiments of this and previous studies (8 runs, 19 data points), with an average $\log_{10}r_1$ value of –1.60±0.25 (in day^{-1}). Similarly, a more limited dataset for the second step (3 runs, 7 data points) displays reasonably close r_2 values, with an average $\log_{10}r_2$ of –2.5±0.2.

The consistency in the derived rate constants for very different experimental setups, solution compositions, and temperatures strongly supports a common universal two-stage mechanism of fluid-pyrite isotope exchange at hydrothermal conditions (Fig. 8). The first stage, controlled by [Fe-HS-S_n] type species, is potentially fast (e.g., according to the r_1 value, <1 month would be required to reach 90% of Fe isotope equilibrium between pyrite and fluid), but is unlikely to go to completion due to very fast pyrite crystal precipitation that blocks the [Fe-HS-S_n] precursor action. The second stage of pyrite re-crystallization takes the lead, and would require more than 1 year to reach 90% of isotope equilibrium, whereas only a few days are necessary for the fluid-pyrite chemical equilibrium to be attained. Therefore, Fe isotope fractionation patterns may record molecular mechanisms of mineral precipitation and recrystallization inaccessible by bulk chemical analyses.

5. Geological significance

Our experimental data at 400–450°C together with those published at 300–350°C (Syverson et al., 2013, 2017) collectively demonstrate that even at such elevated temperatures, kinetic phenomena still control Fe isotope fractionation between aqueous saline fluid and pyrite as they do at lower, close-to-ambient, temperatures. However, at high temperatures, these phenomena are likely to be driven by Fe (poly)sulfide aqueous species precursors, at least at the early stages of pyrite formation, rather than by an intermediate FeS-like phase, as suggested in lower temperature (<100°C) studies (e.g., Butler et al., 2005; Guilbaud et al., 2011; Wu et al., 2012; Mansor and Fantle, 2019). Depending on Fe magnetic spin and coordination, these species, whose exact identity and abundance await further studies, may lead to a variable degree of pyrite depletion in ^{57}Fe relative to the Fe(II) chloride-bearing fluid, in contrast to the expected equilibrium fractionation which should produce ^{57}Fe-enriched pyrite. By providing molecular mechanisms and the associated isotope exchange reaction rates, our data allow an in-depth interpretation of Fe isotope fractionation patterns in natural hydrothermal systems.

For example, measurements of Fe isotope ratios between an Fe-bearing fluid and pyrite precipitating wherefrom at temperatures of 200–450°C in modern seafloor hydrothermal systems (black smokers) all over the world systematically show a significant enrichment of black smoker pyrite in the 'lighter' isotope compared to the coexisting fluid ($\Delta^{57}Fe_{fluid\text{-}pyrite} \approx +0.9$ to +1.5‰; Beard et al., 2003; Rouxel et al., 2003, 2008; Bennett et al., 2009). Our experimental data and model are in agreement with such values, pointing to non-equilibrium isotope fractionation between pyrite and fluid driven by Fe-(poly)sulfide aqueous precursors. Because of the extremely rapid pyrite precipitation rates from an Fe- and H_2S-enriched fluid undergoing a temperature drop at the seafloor, it is very likely that this early pyrite retains the isotope signature of its aqueous (poly)sulfide precursors. Indeed, the pyrite bulk precipitation rates in our and other recent experiments are of an order of hours and thus comparable to those at the seafloor (Rouxel et al., 2008; Bennett et al., 2009). Instead, massive sulfides found in the subsurface oceanic crust, representing reworked remnants of older black smokers, show pyrite samples having lost their 'light' Fe isotope signatures as they re-crystallized and re-equilibrated with the fluid (Rouxel et al., 2008). The rates of such re-equilibration, corresponding to the second stage of the model proposed in our study (Fig. 8), imply durations of at least a year to reach the fluid-pyrite isotope equilibrium (provided *T* and other fluid parameters do not significantly evolve). These durations are comparable to typical time spans of black-smokers activity (Hekinian et al., 1985).

In contrast, pyrites from ancient magmatic-hydrothermal porphyry Cu-Au-Mo, Sn-W, and associated skarn and epithermal deposits, characterized by saline fluids of similar Fe (chloride complexes), and S (coexistence of sulfate and sulfide) speciation to those from MOR, show distinctly 'heavier' δ^{57}Fe signatures (e.g., –0.3 to +1.5‰, Graham et al., 2004; +0.4 to +0.8‰, Li et al., 2018; +0.9 to +1.5‰, Wawryk and Foden, 2015). Such signatures would correspond to a $\Delta^{57}Fe_{fluid\text{-}pyrite}$ value of –1.5‰, assuming that the magmatic-hydrothermal fluid had similar Fe isotope signature as those operating in MOR (e.g., Johnson et al., 2008). This assumption is also supported by the general constancy of the Fe isotope

composition of crustal magmatic rocks ($\delta^{57}Fe$ = 0.10±0.03‰, Poitrasson et al., 2004, 2006). Thus, the negative $\Delta^{57}Fe_{fluid\text{-}pyrite}$ values from magmatic-hydrothermal deposits are more consistent with an equilibrium Fe(aq)-pyrite fractionation estimated from theoretical calculations of this study and previous work (Blanchard et al., 2009; Hill et al., 2010; Rustad et al., 2010; Fuji et al., 2014; Polyakov et al., 2019). Such deposits, usually associated with hydrothermal activity in the proximity of intruded felsic magma bodies in volcanic arc environments, exhibit longer life durations (typically 10–100 ky) and lower *T* gradients, which are favorable for attainment of chemical and isotope equilibrium between fluid and minerals (Barnes, 1997; Graham et al., 2004).

Nevertheless, recent more detailed and spatially resolved investigations of $\delta^{57}Fe$ signatures of pyrite from different ore mineralization stages or various mineral assemblages in hydrothermal deposits yet show a large variability (e.g., Wang et al., 2011; Li et al., 2018; Zhu et al., 2018), which often exceeds that of other coexisting Fe minerals (chalcopyrite, magnetite, pyrrhotite). This distinguishing feature of pyrite isotope systematics may, at least partly, be due to specific kinetic constraints acting on pyrite isotope exchange, by which other Fe sulfide minerals are much less affected (e.g., Polyakov et al., 2007). For example, the rates of Fe isotope equilibration between chalcopyrite and hydrothermal fluid measured at 350°C ($\log_{10}r$ = –0.99 day^{-1}; Syverson et al., 2017) are at least 30 times faster than those of pyrite for the second kinetic stage, implying that only ~10 days would be required for precipitating chalcopyrite to reach Fe isotope equilibrium with the fluid. By contrast, the pyrite Fe isotope exchange rates derived in this study imply that mineralizing events shorter than 1 year, even at temperatures as high as 450°C, may record significant fluid-pyrite Fe isotope disequilibrium, whose extent is strongly dependent on the exact fluid composition and thus the identity of Fe-(poly)sulfide precursor species. Similar time-scale sulfur isotope disequilibria were reported between hydrothermal fluid and pyrite both in nature and laboratory (e.g., Syverson et al., 2015; Kokh et al., 2020), further highlighting strong kinetic controls and the complexity of molecular mechanisms of pyrite precipitation. Disentangling these fundamental molecular-level controls from other temporal and spatial changes in the fluid phase that all affect hydrothermal mineralization in a given natural context (such as different fluid pulses, *T-P* evolution, fluid composition changes, tectonic events), will require integrated studies, combining spatially-resolved Fe, S, and other elements isotope analyses in minerals (and, potentially, fluid inclusions) with more systematic laboratory experiments under controlled conditions, including in-situ spectroscopy, and coupled with molecular modeling approaches.

6. Concluding remarks

This study reports on direct experimental determinations of Fe isotope fractionation between hydrothermal fluid and pyrite over a wide salinity range and at the highest temperatures examined so far (400–450°C, 400–800 bar). Our experiments show a fast attainment, within hours to a few days, of bulk chemical equilibrium between the fluid and pyrite. They provide evidence for the dominant formation of

the aqueous ferrous iron di-chloride $FeCl_2(H_2O)_2^0$ complex, which is the main carrier of Fe in natural hydrothermal fluids and vapors. However, this equilibrium is only "chemical" one because the measured $\Delta^{57}Fe_{fluid\text{-}pyrite}$ values for run durations up to 30 days exhibit a large variability depending on the system composition, but yet remain systematically higher, by 0.5–1.5‰, than the DFT-modeled isotope equilibrium fractionation factors between $FeCl_2(H_2O)_2^0$ and pyrite. These differences provide evidence for significant Fe isotope disequilibrium between fluid and pyrite even at such elevated temperatures.

Combined with the revised and extended theoretical β-factors of Fe sulfide minerals and aqueous species, along with previously available experimental work performed at lower temperatures (300-350°C), our results suggest a new universal two-step model of pyrite formation and isotope equilibration over the hydrothermal *T*-range. The first step, which includes an initial short-term involvement of the lighter Fe isotopes in the reaction of pyrite precipitation, is controlled by Fe (poly)sulfide aqueous species precursors. These species isotopically equilibrate with the fluid dominated by $FeCl_2(H_2O)_2^0$ and transfer their isotope signature without fractionation to the rapidly precipitating pyrite. This signature depends on the exact identity of the precursor species, Fe electronic state (low or high spin) and coordination, leading to a large variability of the resulting $\Delta^{57}Fe_{fluid\text{-}pyrite}$ values. This step is fast (<1 month would be enough to attain 90% of true fluid-pyrite Fe isotope equilibrium), but is blocked before reaching equilibrium owing to the continued pyrite growth thereby preserving the initially acquired $\Delta^{57}Fe_{fluid\text{-}pyrite}$ value. This step is followed by a much slower second step of pyrite re-crystallization and re-equilibration with the fluid that should require on average about 1 year to attain isotope equilibrium.

The fluid-pyrite fractionation factors and exchange rates of Fe isotopes derived in this study are in agreement with those from active seafloor hydrothermal fields that are characterized by rapid pyrite precipitation rates and apparent Fe isotope disequilibrium leading to δ^{57}Fe-depleted pyrites relative to the fluid. Our model also accounts well for the generally δ^{57}Fe-enriched signatures of pyrite from magmatic-hydrothermal deposits that have been formed by similar saline S-bearing fluids but over longer periods of time, sufficient to attain fluid-pyrite isotope equilibrium. Our results offer a new interpretation of Fe isotope variabilities in pyrite in terms of molecular-level kinetic control and the amplitude of isotope disequilibrium that may help better tracing relatively short-term mineralizing events inaccessible by traditional approaches.

Acknowledgements

This research was funded by the French Ministère de l'Education Nationale et de la Recherche and University of Toulouse III Paul Sabatier (PhD fellowship and Action Innovante du Conseil Scientifique de l'Université Paul Sabatier, grant ISOFER to F.P.), by the Programme National de Planétologie (PNP) of CNRS-INSU co-funded by CNES (to F.P.), and by the Agence Nationale de la Recherche (grants RadicalS - ANR-16-CE31-0017 and ISIFoR - OrPet to G.S.P). Calculations were performed using the HPC resources from CALMIP (grant 2020 - P1037 to M.B.). We thank Jerôme Chmeleff for his furious energy in repairing all failures of the MC-ICP-MS machine. We are grateful to Thierry Aigouy for SEM analyses, Michel Thibaut for DRX analyses, Carole Causserand for AAS analyses, Anne-Marie Cousin for help with figure preparation, Jonathan Prunier, Carole Boucayrand and Manuel Henry for assistance in the clean room, Veniamin Polyakov and Etienne Balan for discussions on iron isotope fractionation, and Drew Syverson for sharing experimental data. Constructive comments of Associate Editor Chen Zhu and two anonymous reviewers greatly improved this article.

References

Akinfiev N. N. and Diamond L. W. (2003) Thermodynamic description of aqueous nonelectrolytes over a wide range of state parameters. *Geochim. Cosmochim. Acta* **67**, 613-627.

Anbar A. D., Jarzecki A. A. and Spiro T. G. (2005) Theoretical investigation of iron isotope fractionation between $Fe(H_2O)_6^{3+}$ and $Fe(H_2O)_6^{2+}$: Implications for iron stable isotope geochemistry. *Geochim. Cosmochim. Acta* **69**, 825-837.

Antonov V. N., Bekenov L. V., Shpak A. P., Germash L. P., Yaresko A. N. and Jepsen O. (2009) X-ray magnetic circular dichroism in iron chalcogenides $Fe_{1-x}S$: First-principles calculations. *J. Applied Phys*. **106**, 123907.

Avril C., Malavergne V., Caracas R., Zanda B., Reynard B., Charon E., Bobocioiu E., Brunet F., Borensztajn S., Pont S., Tarrida M., Guyot F. (2013) Raman spectroscopic properties and Raman identification of CaS-MgS-MnS-FeS-Cr_2FeS_4 sulfides in meteorites and reduced sulfur-rich systems. *Meteorit. Planet. Sci*. **48**, 1415–1426.

Baes C. F. Jr. and Mesmer R. E. (1976). *The Hydrolysis of Cations*. Wiley.

Barnes H. L. (1997) *Geochemistry of Hydrothermal Ore Deposits*. New York, Wiley.

Bazarkina E. F., Pokrovski G. S., Zotov A. V. and Hazemann J-L. (2010) Structure and stability of cadmium chloride complexes in hydrothermal fluids. *Chem. Geol*. **276**, 1–17.

Beard B. L., Johnson C. M., Von Damm K. L. and Poulson R. L. (2003) Iron isotope constraints on Fe cycling and mass balance in oxygenated Earth oceans. *Geology* **31**, 629–632.

Becke A. D. (1993) Density functional thermochemistry. 3. The role of exact exchange. *J. Chem. Phys*. **98**, 5648–5652.

Bennett S. A.., Rouxel O., Schmidt K., Garbe-Schönberg D., Statham P. J. and German C. R. (2009) Iron isotope fractionation in a buoyant hydrothermal plume, 5°S Mid-Atlantic Ridge. *Geochim. Cosmochim. Acta* **73**, 5619–5634.

Bigeleisen J. and Mayer M. G. (1947) Calculation of equilibrium constants for isotopic exchange reactions. *J. Chem. Phys*. **15**, 261–267.

Blanchard M., Poitrasson F., Méheut M., Lazzeri M., Mauri F. and Balan E. (2009) Iron isotope fractionation between pyrite (FeS_2), hematite (Fe_2O_3) and siderite ($FeCO_3$): A first-principles density functional theory study. *Geochim. Cosmochim. Acta* **73**, 6565–6578.

Blanchard M., Poitrasson F., Méheut M., Lazzeri M., Mauri F. and Balan E. (2012) Comment on "New data on equilibrium iron isotope fractionation among sulfides: Constraints on the mechanisms of sulfide formation in hydrothermal and igneous systems" by V.B. Polyakov and D.M. Soultanov. *Geochim. Cosmochim. Acta* **87**, 356–359.

Blanchard M., Balan E. and Schauble E. (2017) Equilibrium fractionation of non-traditional isotopes: a molecular modeling perspective. *Rev. Mineral. Geochem*. **82**, 27–63.

Brostigen G. and Kjekshus A. (1969) Redetermined crystal structure of FeS_2 (pyrite). *Acta Chem. Scand*. **23**, 2186–2188.

Buerger M. (1937) Interatomic distances in marcasite and notes on the bonding in crystals of loellingite, arsenopyrite, and marcasite types. *Zeit. Kristallogr*. **97**, 504–513.

Butler I. B., Archer C., Vance D., Oldroyd A. and Rickard D. (2005) Fe isotope fractionation on FeS formation in ambient aqueous solution. *Earth Planet Sci. Lett*. **236**, 430–442.

Chase M. W. Jr. (1998) NIST-JANAF Thermochemical Tables, Fourth Edition. *J. Phys. Chem. Ref. Data,* Monograph **9**, 1–1951.

Cheng Y. B., Mao J. W., Zhu X. K. and Wang Y. (2015) Iron isotope fractionation during supergene weathering process and its application to constrain ore genesis in Gaosong deposit, Gejiu district, SW China. *Gondwana Res*. **27**, 1283–1291.

Chivers T. and Elder P. J. W. (2013) Ubiquitous trisulfur radical ion: fundamentals and applications in materials science, electrochemistry, analytical chemistry and geochemistry. *Chem. Soc. Rev*. **42**, 5996–6005.

Cole D. R. and Chakraborty S. (2001). Rates and mechanisms of isotopic exchange. *Rev. Miner. Geochem*. **43**, 83–223.

Colin A., Schmidt C., Pokrovski G. S., Wilke M., Borisova A. Y. and Toplis M. (2020) *In situ* determination of sulfur speciation and partitioning in aqueous fluid-silicate melt systems. *Geochem. Persp. Lett*. **14**, 31–35.

Crerar D., Wood S. and Brantley S. (1985) Chemical controls on solubility of ore-forming minerals in hydrothermal solutions. *Can. Mineral*. **23**, 333–352.

Dal Corso A. (2014) Pseudopotentials periodic table: From H to Pu. *Comput. Mater. Sci*. **95**, 337–350.

Domagal-Goldman S. D. and Kubicki J. D. (2008) Density functional theory predictions of equilibrium isotope fractionation of iron due to redox changes and organic complexation. *Geochim. Cosmochim. Acta* **72**, 5201–5216.

Dauphas N., Roskosz M., Alp E., Golden D., Sio C., Tissot F., Hu M., Zhao J., Gao L. and Morris R. (2012) A general moment NRIXS approach to the determination of equilibrium Fe isotopic fractionation factors: application to goethite and jarosite. *Geochim. Cosmochim. Acta* **94**, 254−275.

Dauphas N., John S. G. and Rouxel O. (2017) Iron isotope systematics. *Rev. Mineral. Geochem*. **82**, 415–510.

El Mendili Y., Minisini B., Abdelouas A. and Bardeau J-F. (2014) Assignment of Raman-active vibrational modes of tetragonal mackinawite: Raman investigations and ab-initio calculations. *RSC Advances* **4**, 25827–25834.

Einaudi M.T., Hedenquist J.W. and Inan E.E. (2003) Sulfidation state of fluids in active and extinct hydrothermal systems: transitions from porphyry to epithermal environments (eds. S.F. Simmons and I.J. Graham). *Soc. Econ. Geol. Spec. Publ.* **10**, 285-313.

Frisch M. J., Trucks G. W., Schlegel H. B. et al. (2016) *Gaussian 16, Revision B.01*, Gaussian, Inc., Wallingford CT

Fujii T., Moynier F., Blichert-Toft J. and Albarede F. (2014) Density functional theory estimation of isotope fractionation of Fe, Ni, Cu, and Zn among species relevant to geochemical and biological environments. *Geochim. Cosmochim. Acta* **140**, 553–576.

Giannozzi P., Baroni S., Bonini N. et al. (2009) QUANTUM ESPRESSO: a modular and open-source software project for quantum simulations of materials. *J. Phys. Condens. Mat*. **21**, 395502.

Graham S., Pearson N., Jackson S., Griffin W., O'Reilly S. Y. (2004) Tracing Cu and Fe from source to porphyry: in situ determination of Cu and Fe isotope ratios in sulfides from the Grasberg Cu-Au deposit. *Chem. Geol*. **207**, 147–169.

Guilbaud R., Butler I. B., Ellam R. M. and Rickard D. (2010) Fe isotope exchange between $Fe(II)_{aq}$ and nanoparticulate mackinawite (FeS_m) during nanoparticle growth. *Earth Planet. Sci. Lett*. **300**, 174–183.

Guilbaud R., Butler I. B., Ellam R. M., Rickard D. and Oldroyd A. (2011) Experimental determination of the equilibrium Fe isotope fractionation between Fe^{2+}_{aq} and FeS_m (mackinawite) at 25 and 2 °C. *Geochim. Cosmochim. Acta* **75**, 2721–2734.

Heimann A., Beard B. and Johnson C. (2008) The role volatile exsolution and sub-solidus fluid/rock interactions in producing high $^{56}Fe/^{54}Fe$ ratios in siliceous igneous rocks. *Geochim. Cosmochim. Acta*. **72**, 4379–4396.

Hekinian R., Francheteau J. and Ballard R. D. (1985) Morphology and evolution of hydrothermal deposits at the axis of the East Pacific Rise. *Oceanol. Acta* **8**, 147–155.

Hill P. S. and Schauble E. A. (2008) Modeling the effects of bond environment on equilibrium iron isotope fractionation in ferric aquo-chloro complexes. *Geochim. Cosmochim. Acta* **72**, 1939–1958.

Hill P. S., Schauble E. A. and Young E. D. (2010) Effects of changing solution chemistry on Fe^{3+}/Fe^{2+} isotope fractionation in aqueous Fe-Cl solutions. *Geochim. Cosmochim. Acta* **74**, 6669–6689.

Hoefs J. (2015) *Stable Isotope Geochemistry*. Springer-Verlag, Berlin, 389 pp.

Johnson C. M., Beard B. and Roden E. (2008) The iron isotope fingerprints of redox and biogeochemical cycling in modern and ancient Earth. *Ann. Rev. Earth Planet. Sci*. **36**, 457–493.

Johnson J. W., Oelkers E.H. and Helgeson H. C. (1992) SUPCRT92 , A software package for calculating the standard molal thermodynamic properties of minerals, gases, aqueous species, and reactions from 1 to 5000 bar and 0 to 1000°C. *Comput. Geosci*. **18**, 899–947, http//geopig.asu.edu/index.html#.

Kokh M. A., Akinfiev N. N., Pokrovski G. S., Salvi S. and Guillaume D. (2017) The role of carbon dioxide in the transport and fractionation of metals by geological fluids. *Geochim. Cosmochim. Acta* **197**, 433–466.

Kokh M. A., Assayag N., Mounic S., Cartigny P., Gurenko A. and Pokrovski G. S. (2020) Multiple sulfur isotope fractionation in hydrothermal systems in the presence of radical ions and molecular sulfur. *Geochim. Cosmochim. Acta* **285**, 100–128.

Kouzmanov K. and Pokrovski G.S. (2012) Hydrothermal controls on metal distribution in Cu(-Au-Mo) porphyry systems. In: 'Geology and Genesis of Geology and Genesis of Major Copper Deposits and Districts of the World: A Tribute to Richard H. Sillitoe' (eds. J.W. Hedenquist, M. Harris, and F. Camus). *Soc. Econ. Geol. Spec. Publ.* **16**, 573–618.

Kwon K. D., Refson K., Bone S., Qiao R., Yang W-L., Liu Z. and Sposito G. (2011) Magnetic ordering in tetragonal FeS: Evidence for strong itinerant spin fluctuations. *Phys. Rev*. **B83**, 064402.

Lee C. T., Yang W. T. et al. (1988) Development of the Colle-Salvetti correlation-energy formula into a functional of the electron-density. *Phys. Rev*. **B37**, 785–789.

Lennie A. R., Redfern S. A. T., Schofield P. F. and Vaughan D. J. (1995) Synthesis and Rietveld crystal structure refinement of mackinawite, tetragonal FeS. *Miner. Mag*. **59**, 677–683.

Li J. X., Qin K. Z., Li G. M., Evans N. J., Huang F. and Zhao J. X. (2018) Iron isotope fractionation during magmatic-hydrothermal evolution: A case study from the Duolong porphyry Cu-Au deposit, Tibet. *Geochim. Cosmochim. Acta* **238**, 1–15.

Luther G. W. III, Theberge S. M. and Richard D. T. (1999) Evidence for aqueous clusters as intermediates during zinc sulfide formation. *Geochim. Cosmochim. Acta* **63**, 3159–3169.

Mansor M. and Fantle M. S. (2019) A novel framework for interpreting pyrite-based Fe isotope records of the past. *Geochim. Cosmochim. Acta* **253**, 39–62.

Markl G., von Blanckenburg F. and Wagner T. (2006) Iron isotope fractionation during hydrothermal ore deposition and alteration. *Geochim. Cosmochim. Acta* **70**, 3011–3030.

Méheut M., Lazzeri M., Balan E. and Mauri F. (2009) Structural control over equilibrium silicon and oxygen isotopic fractionation: A first-principles density-functional theory study. *Chem. Geol*. **258**, 28–37.

Monkhorst H. J. and Pack J. D. (1976) Special points for Brillouin zone integrations. *Phys. Rev*. **B13**, 5188–5192.

Murowchick J. B. and Barnes H. L. (1986) Marcasite precipitation from hydrothermal solutions. *Geochim. Cosmochim. Acta* **50**, 2615–2629.

Oelkers E. H., Benezeth P. and Pokrovski G. S. (2009) Thermodynamic databases for water-rock interaction. In: Thermodynamics and kinetics of water-rock interactions. *Rev. Miner. Geochem*. **70**, 1–46.

Perdew J. P., Burke K. and Ernzerhof M. (1996) Generalized gradient approximation made simple. *Phys. Rev. Lett.* **77**, 3865–3868.

Pi Q. H., Zhong R. C. and Hu R. Z. (2015) Tracing the ore-formation history of the shear-zone-controlled Huogeqi Cu-Pb-Zn deposit in Inner Mongolia, northern China, using H, O, S, and Fe isotopes. *Ore Geol. Rev*. **71**, 263–272.

Platzner I. T. (1997) *Modern Isotope Ratio Mass Spectrometry*. JohnWiley & Sons, Chichester, 1–514.

Poitrasson F. (2006) On the iron isotope homogeneity level of the continental crust. *Chem. Geol*. **235**, 195–200.

Poitrasson F. and Freydier R. (2005) Heavy iron isotope composition of granites determined by high resolution MC-ICP-MS. *Chem. Geol*. **222**, 132-147.

Poitrasson F., Halliday A. N., Lee D-C., Levasseur S. and Teutsch N. (2004) Iron isotope differences between Earth, Moon, Mars and Vesta as possible records of contrasted accretion mechanisms. *Earth Planet. Sci. Lett.* **223**, 253–266.

Pokrovski G. S. and Dubrovinsky L. S. (2011) The S_3^- ion is stable in geological fluids at elevated temperatures and pressures. *Science* **331**, 1052–1054.

Pokrovski G. S. and Dubessy J. (2015) Stability and abundance of the trisulfur radical ion S_3^- in hydrothermal fluids. *Earth Planet. Sci. Lett*. **411**, 298–309.

Pokrovski G. S., Borisova A. Y. and Harrichoury J-C. (2008) The effect of sulfur on vapor-liquid fractionation of metals in hydrothermal systems. *Earth Planet. Sci. Lett*. **266**, 345–362.

Pokrovski G. S., Tagirov B. R., Schott J., Hazemann J-L. and Proux O. (2009) A new view on gold speciation in sulfur-bearing hydrothermal fluids from in situ X-ray absorption spectroscopy and quantum chemical modelling. *Geochim. Cosmochim. Acta* **73**, 5406–5427.

Pokrovski G. S., Borisova A. Y. and Bychkov A. Y. (2013) Speciation and transport of metals and metalloids in geological vapors. *Rev. Miner. Geochem*. **76**, 165–218.

Pokrovski G. S., Kokh M. A., Guillaume D., Borisova A. Y., Gisquet P., Hazemann J.-L., Lahera E., Del Net W., Proux O., Testemale D., Haigis V., Jonchière R., Seitsonen A. P., Ferlat G., Vuilleumier R., Saitta A. M., Boiron M.-C. and Dubessy J. (2015). Sulfur radical species form gold deposits on Earth. *Proc. Nat. Acad. Sci USA* **112**, 13484–13489.

Pokrovski G. S., Kokh M. A., Proux O., Hazemann J-L., Bazarkina E. F., Testemale D., Escoda C., Boiron M-C., Blanchard M., Aigouy T., Gouy S., de Parseval P. and Thibaut M. (2019) The nature and partitioning of invisible gold in the pyrite-fluid system. *Ore Geol. Rev*. **109**, 545–563.

Polyakov V. B. (2009) Equilibrium iron isotope fractionation at core-mantle boundary conditions. *Science* **323**, 912–914.

Polyakov V. B. and Mineev S. D. (2000) The use of Mössbauer spectroscopy in stable isotope geochemistry. *Geochim. Cosmochim. Acta* **64**, 849–865.

Polyakov V. B. and Soultanov D. M. (2011) New data on equilibrium iron isotope fractionation among sulfides: Constraints on mechanisms of sulfide formation in hydrothermal and igneous systems. *Geochim. Cosmochim. Acta* **75**, 1957–1974.

Polyakov V. B., Clayton R. N., Horita J. and Mineev S. D. (2007) Equilibrium iron isotope fractionation factors of minerals: Reevaluation from the data of nuclear inelastic resonant X-ray scattering and Mössbauer spectroscopy. *Geochim. Cosmochim. Acta* **71**, 3833–3846.

Polyakov V. B., Osadchii E., Chareev D., Chumakov A. and Sergeev I. (2013) Fe β-factors for sulfides from NRIXS synchrotron experiments. *Mineral. Mag*. **77**, 1985.

Polyakov V. B., Osadchii E. G., Voronin M. V., Osadchii V. O., Sipavina L. V., Chareev D. A., Tyurin A. V., Gurevich V. M. and Gavrichev K. S. (2019) Iron and sulfur isotope factors of pyrite: data from experimental Mossbauer spectroscopy and heat capacity. *Geochem. Intern*. **57**, 369–383.

Rickard D. and Luther G. W. III (2007) Chemistry of iron sulfides. *Chem. Rev*. **107**, 514–562.

Robie R. A. and Hemingway B. S. (1995) Thermodynamic properties of minerals and related substances at 298.15 K and 1 bar (10^5 Pascals) pressure and at higher temperatures. *US Geol. Survey Bull.* **2131**, 1–461.

Rodushkin I., Stenberg A., Andrén H., Malinovsky D. and Baxter D. C. (2004) Isotopic fractionation during diffusion of transition metal ions in solution. *Anal. Chem*. **76**, 2148–2151.

Rouxel O., Dobbek N., Ludden J. and Fouquet Y. (2003) Iron isotope fractionation during oceanic crust alteration. *Chem. Geol*. **202**, 155–182.

Rouxel O., Fouquet Y. and Ludden J. N. (2004) Subsurface processes at the lucky strike hydrothermal field, Mid-Atlantic ridge: evidence from sulfur, selenium, and iron isotopes. *Geochim. Cosmochim. Acta* **68**, 2295–2311.

Rouxel O., Shanks W. C., Bach W. and Edwards K. J. (2008) Integrated Fe- and S-isotope study of seafloor hydrothermal vents at East Pacific Rise 9–10°N. *Chem. Geol*. **252**, 214–227.

Rustad J. R. and Dixon D. A. (2009). Prediction of iron-isotope fractionation between hematite (α-Fe_2O_3) and ferric and ferrous iron in aqueous solution from density functional theory. *J. Phys. Chem. A* **113**, 12249-12255.

Rustad J. R., Casey W. H., Yin Q-Z., Bylaska E. J., Felmy A. R., Bogatko S. A., Jackson V. E. and Dixon D. A. (2010) Isotopic fractionation of Mg^{2+}(aq), Ca^{2+}(aq), and Fe^{2+}(aq) with carbonate minerals. *Geochim. Cosmochim. Acta* **74**, 6301–6323.

Saunier G., Pokrovski G. S. and Poitrasson F. (2011) First experimental determination of iron isotope fractionation between hematite and aqueous solution at hydrothermal conditions. *Geochim. Cosmochim. Acta* **75**, 6629–6654.

Schauble E. A., Rossman G. R. and Taylor H. P. (2001) Theoretical estimates of equilibrium Fe-isotope fractionations from vibrational spectroscopy. *Geochim. Cosmochim. Acta* **65**, 2487–2497.

Scholten L., Schmidt C., Lecumberri-Sanchez P., Newville M., Lanzirotti A., Sirbescu M.-L. C. and Steele-MacInnis M. (2019) Solubility and speciation of iron in hydrothermal fluids. *Geochim. Cosmochim. Acta* **252**, 126–143.

Schoonen M. A. and Barnes H. L. (1991) Mechanisms of pyrite and marcasite formation from solution: III. Hydrothermal processes. *Geochim. Cosmochim. Acta* **55**, 3491–3504.

Seyfried W. E., Janecky D. R. and Berndt M. E. (1987) Rocking autoclaves for hydrothermal experiments II. The flexible reaction-cell system. In *Hydrothermal Experimental Techniques* (eds. G.C. Ulmer and H.L. Barnes). John Wiley & Sons, Inc., New York. pp. 216–239.

Sharma M., Polizzotto M. and Anbar A. D. (2001) Iron isotopes in hot springs along the Juan the Fuca Ridge. *Earth Planet. Sci. Lett*. **194**, 39–51.

Shock E. L., Sassani D. C., Willis M. and Sverjensky D. A. (1997) Inorganic species in geologic fluids: Correlations among standard molal thermodynamic properties of aqueous ions and hydroxide complexes. *Geochim. Cosmochim. Acta* **61**, 907–950.

Shvarov Y. V. (2008) HCh: New potentialities for the thermodynamic simulation of geochemical systems offered by Windows. *Geochem. Intern*. **46**, 834–839.

Shvarov Y. V. (2015) A suite of programs, OptimA, OptimB, OptimC, and OptimS, compatible with the Unitherm database, for deriving the thermodynamic properties of aqueous species from solubility, potentiometry and spectroscopy measurements. *Applied Geochem*. **55**, 17–27.

Skala R., Cisarova I. and Drabek M. (2006) Inversion twinning in troilite. *Amer. Mineral*. **91**, 917–921.

Skulan J. L., Beard B. L. and Johnson C. M. (2002) Kinetic and equilibrium Fe isotope fractionation between aqueous Fe(III) and hematite. *Geochim. Cosmochim. Acta* **66**, 2995–3015.

Stefánsson A., Lemke K. H. and Seward T. M. (2019) Iron(III) chloride complexation in hydrothermal solutions , A combined spectrophotometric and density functional theory study. *Chem. Geol*. **524**, 77–87.

Sverjensky D. A., Shock E. L. and Helgeson H. C. (1997) Prediction of the thermodynamic properties of aqueous metal complexes to 1000°C and 5 kb. *Geochim. Cosmochim. Acta* **61**,1359–1412.

Sverjensky D. A., Harrison B. and Azzolini D. (2014) Water in the deep Earth: the dielectric constant and the solubilities of quartz and corundum to 60 kb and 1200°C. *Geochim. Cosmochim. Acta* **129**, 125–145.

Syverson D. D., Borrok D. M. and Seyfried W. E. (2013) Experimental determination of equilibrium Fe isotopic fractionation between pyrite and dissolved Fe under hydrothermal conditions. *Geochim. Cosmochim. Acta* **122**, 170–183.

Syverson D. D., Pester N.J., Craddock P.R. and Seyfried W. E. Jr. (2014) Fe isotope fractionation during phase separation in the NaCl-H_2O system. An experimental study with implications for seafloor hydrothermal vents. *Earth Planet. Sci. Lett*. **406**, 223–232.

Syverson D. D., Ono S., Shanks W. C. and Seyfried W. E. Jr. (2015) Multiple sulfur isotope fractionation and mass transfer processes during pyrite precipitation and recrystallization: An experimental study at 300 and 350°C. *Geochim. Cosmochim. Acta* **165**, 418–434.

Syverson D. D., Luhmann A. J., Tan C., Borrok D. M., Ding K. and Seyfried W. E. Jr. (2017) Fe isotope fractionation between chalcopyrite and dissolved Fe during hydrothermal recrystallization: An experimental study at 350 °C and 500 bars. *Geochim. Cosmochim. Acta* **200**, 87–109.

Testemale D., Brugger J., Liu W., Etschmann B. and Hazemann J-L. (2009) In-situ X-ray absorption study of iron(II) speciation in brines up to supercritical conditions. *Chem. Geol*. **264**, 295–310.

Wang Y., Zhu X. K., Mao J. W., Li Z. H. and Cheng Y. B. (2011) Iron isotope fractionation during skarn-type metallogeny: A case study of Xinqiao Cu-S-Fe-Au deposit in the Middle-Lower Yangtze valley. *Ore Geol. Rev*. **43**, 194–202.

Watkins J. M., DePaolo D. J. and Watson E. B. (2017) Kinetic fractionation of non-traditional stable isotopes by diffusion and crystal growth reactions. *Rev. Mineral. Geochem*. **82**, 85–125.

Wawryk C. M. and Foden J. D. (2015) Fe-isotope fractionation in magmatic-hydrothermal mineral deposits: A case study from the Renison Sn-W deposit, Tasmania. *Geochim. Cosmochim. Acta* **150**, 285–298.

Wiesli R. A., Beard B.L. and Johnson C. M. (2004) Experimental determination of Fe isotope fractionation between aqueous Fe(II), siderite and "green rust" in abiotic systems. *Chem. Geol.* **211**, 343–362.

Wood S. A. and Samson I. M. (1998). Solubility of ore minerals and complexation of ore metals in hydrothermal solutions. *Rev. Econ. Geol*. **10**, 33–77.

Wu L. L., Druschel G., Findlay A., Beard B. L. and Johnson C. M. (2012) Experimental determination of iron isotope fractionations among $Fe_{aq}^{(2+)}$-FeS_{aq}-Mackinawite at low temperatures: Implications for the rock record. *Geochim. Cosmochim. Acta* **89**, 46–61.

Zhu B., Zhang H. F., Zhao X. M. and He Y. S. (2016) Iron isotope fractionation during skarn-type alteration: Implications for metal source in the Han-Xing iron skarn deposit. *Ore Geol. Rev*. **74**, 139–150.

Zhu Z-Y., Jiang S-Y., Mathur R., Cook N.J., Yang T., Wang M., Ma L. and Ciobanu C. L. (2018) Iron isotope behavior during fluid/rock interaction in K-feldspar alteration zone – A model for pyrite in gold deposits from the Jiaodong Peninsula, East China. *Geochim. Cosmochim. Acta* **222**, 94–116.

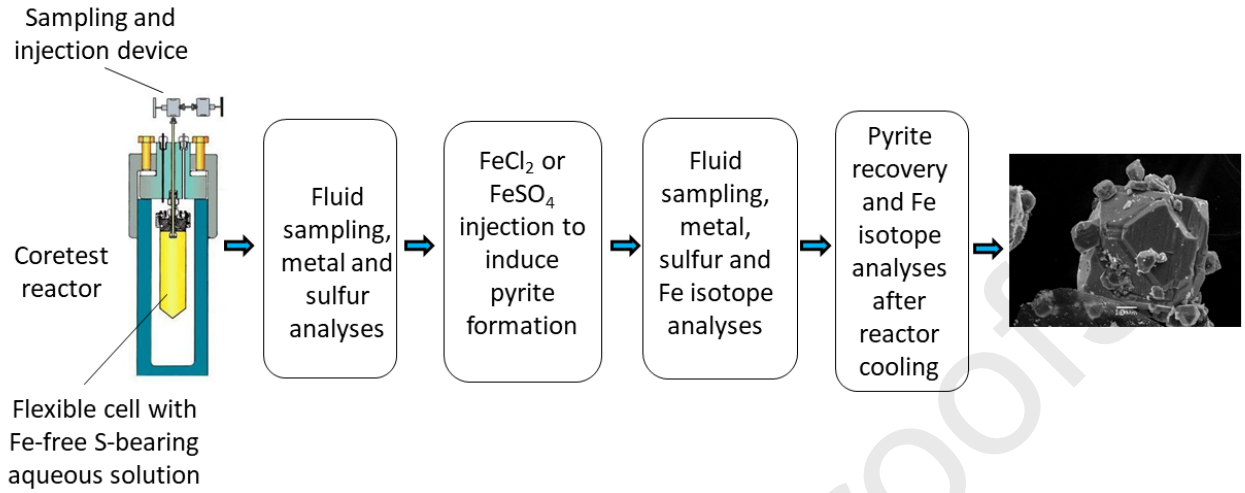

Figure 1. Sequence of the main experimental and analytical steps of this study to investigate Fe isotope fractionation during in-situ induced pyrite precipitation from hydrothermal fluid.

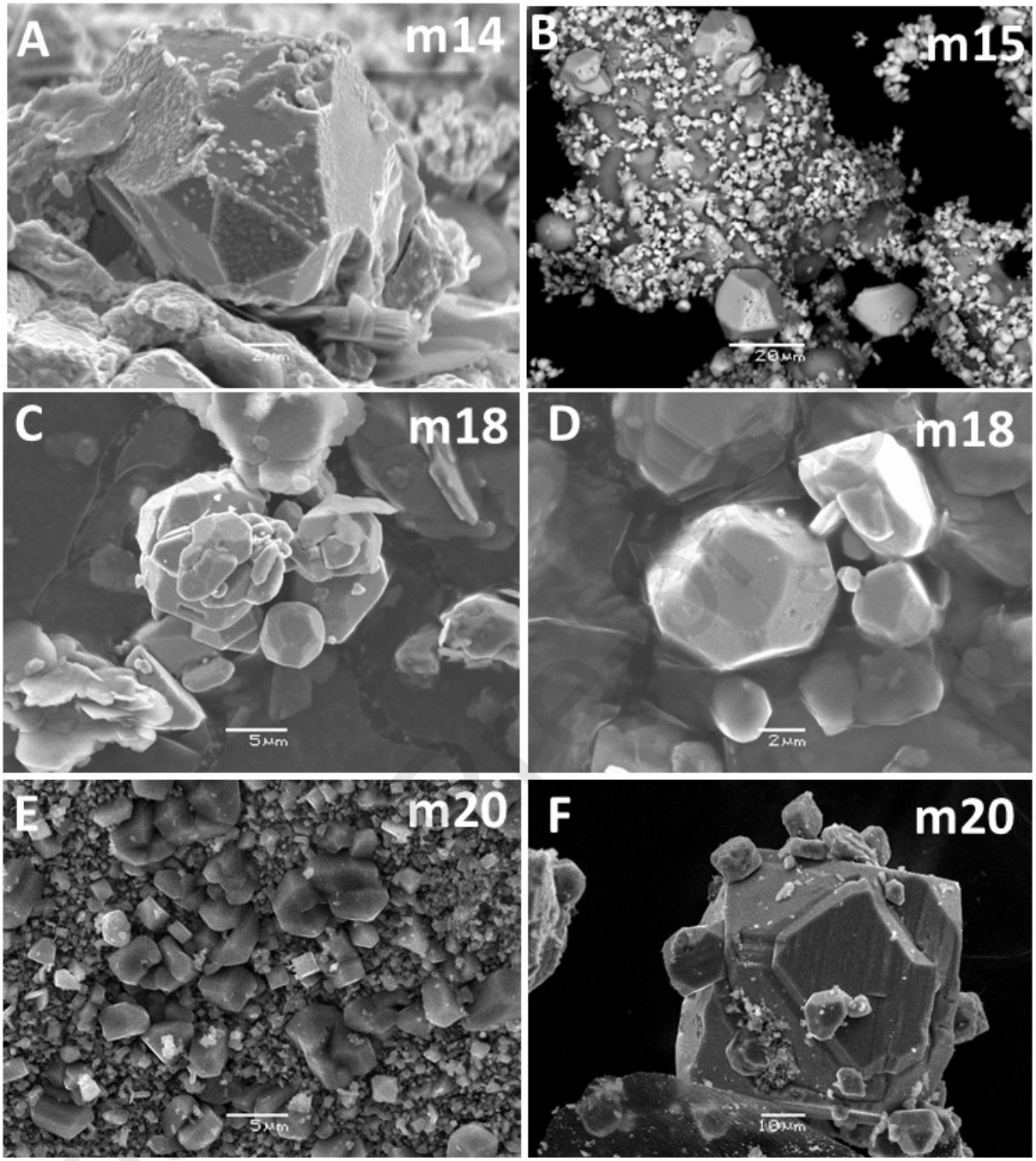

Figure 2. Scanning electron microscopy microphotographs of pyrite after the precipitation experiments of this study (in backscattered, BE, or secondary, SE, electron modes). (A) A pyritohedron-habit (i.e. pentagonal faces, {201}) pyrite crystal with nano-sized gold particles precipitated on its faces in experiment m14 (SE); (B) a few large (10-20 μm) pyrite crystals of mixed cubic {100} and octahedral {111} habit together with smaller particles agglomerated on native sulfur, which was deposited on cooling in m15 (BE); (C) and (D) variable-size (<1 μm to 10 μm) pyrite crystals of mixed pyritohedron-cubic habit in m18 (SE); (E) variable-size cubic and octahedral pyrite crystals composing the whole precipitated solid in m20 (BE); (F) a zoom on a large pyrite crystal (~50 μm) of predominantly cubic shape with remnants of octahedral (triangular-shape) faces in m20 (BE).

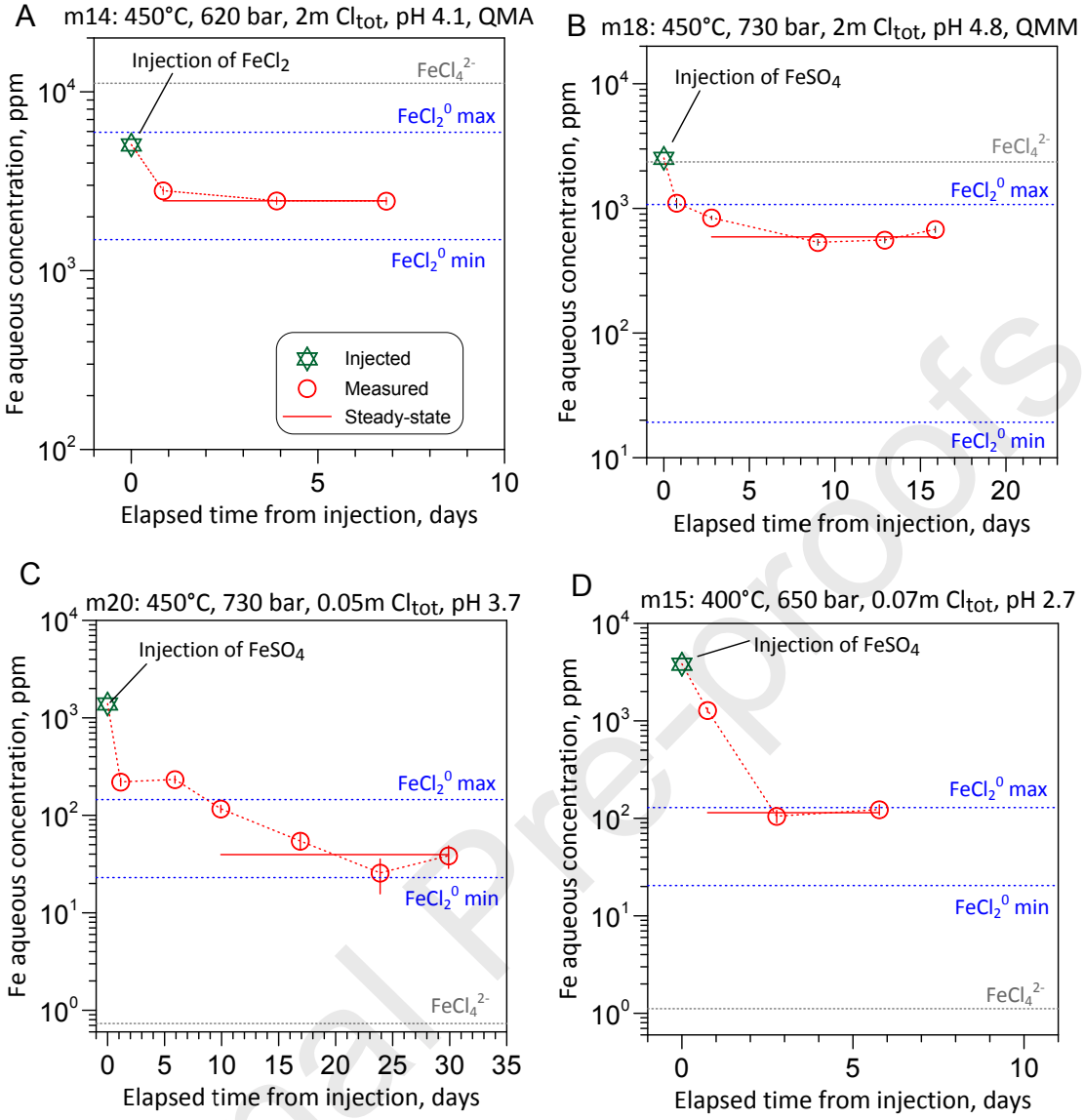

Figure 3. Total aqueous Fe concentrations (red circles) as a function of time in the four precipitation experiments at the indicated conditions (see Table B.1 for numerical data). The green star shows the total concentration of Fe in the system right after the injection of a $FeCl_2$ or $FeSO_4$ aqueous solution into the Fe-free S-bearing fluid, after which Fe aqueous concentrations drop due to pyrite precipitation. The horizontal solid red line shows the steady-state Fe concentrations calculated as the average of measured concentrations that do not show systematic time-dependent trends. The horizontal dashed blue lines delimit the range of the $FeCl_2^0$ complex concentrations (min and max) taking account of the associated uncertainties as calculated assuming chemical equilibrium with pyrite and using the thermodynamic data of aqueous Fe^{II} chloride species from Sverjensky et al. (1997), whereas the horizontal dashed gray line indicates possible mean concentrations of the $FeCl_4^{2-}$ complex that could be roughly estimated using its stability constants from Testemale et al. (2009). The concentrations of Fe^{III} chloride species estimated according to equilibrium constants reported in Saunier et al. (2011) are less than 0.1 ppb Fe at the experimental conditions of this study.

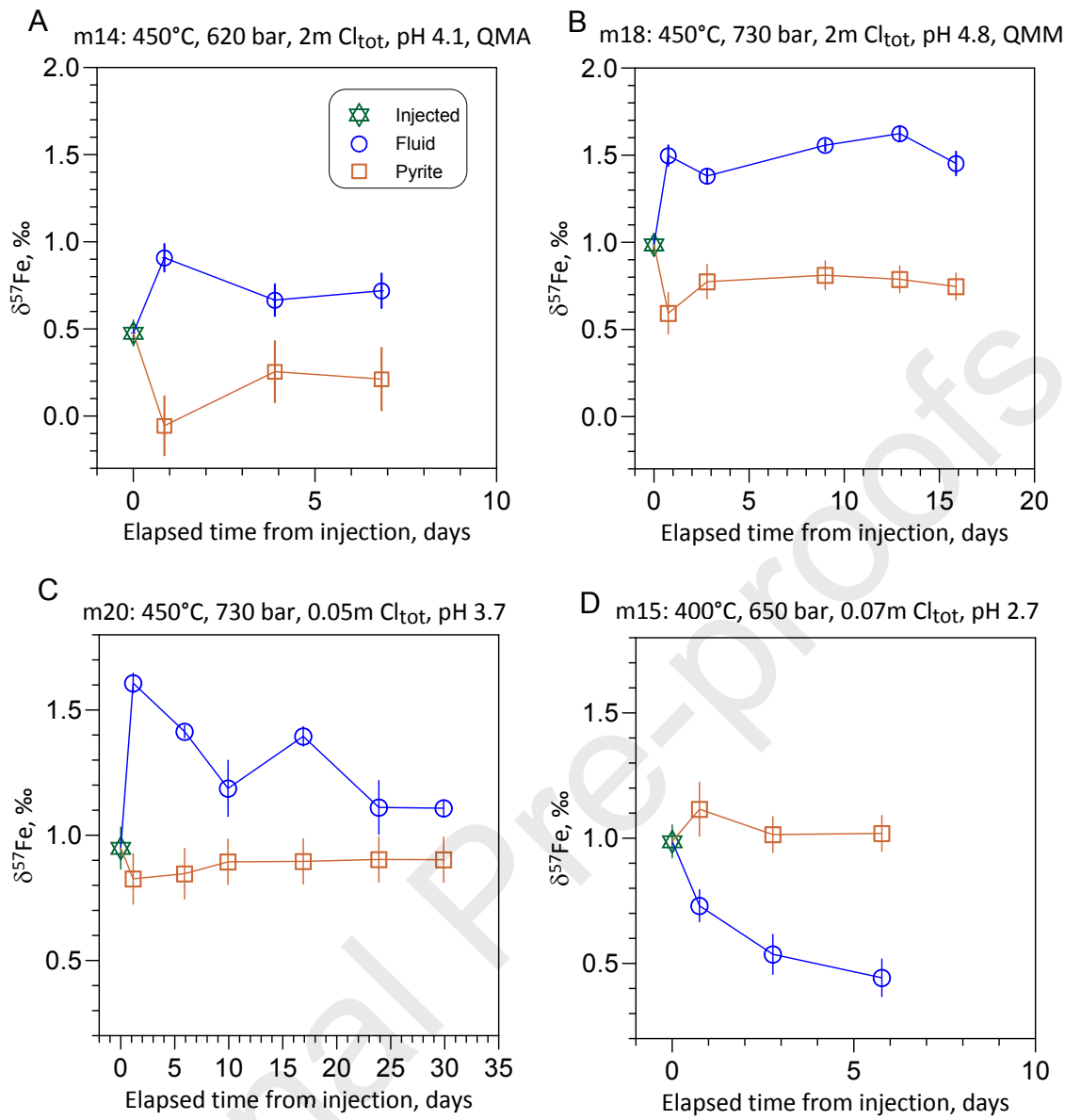

Figure 4. Iron isotope composition (in δ^{57}Fe relative to IRMM-014) of the initial injected Fe-bearing solution, the coexisting aqueous fluid, and pyrite as a function of time in the experiments of this study at indicated conditions. The δ^{57}Fe values of the fluid after pyrite precipitation (blue circles) were directly measured in the fluid samples; those of pyrite (brown squares) were derived using mass balance between the initial, sampled, and injected amounts of fluid and the measured $\delta^{57}Fe_{fluid}$ at each sampling step (see Table 2 for data and details).

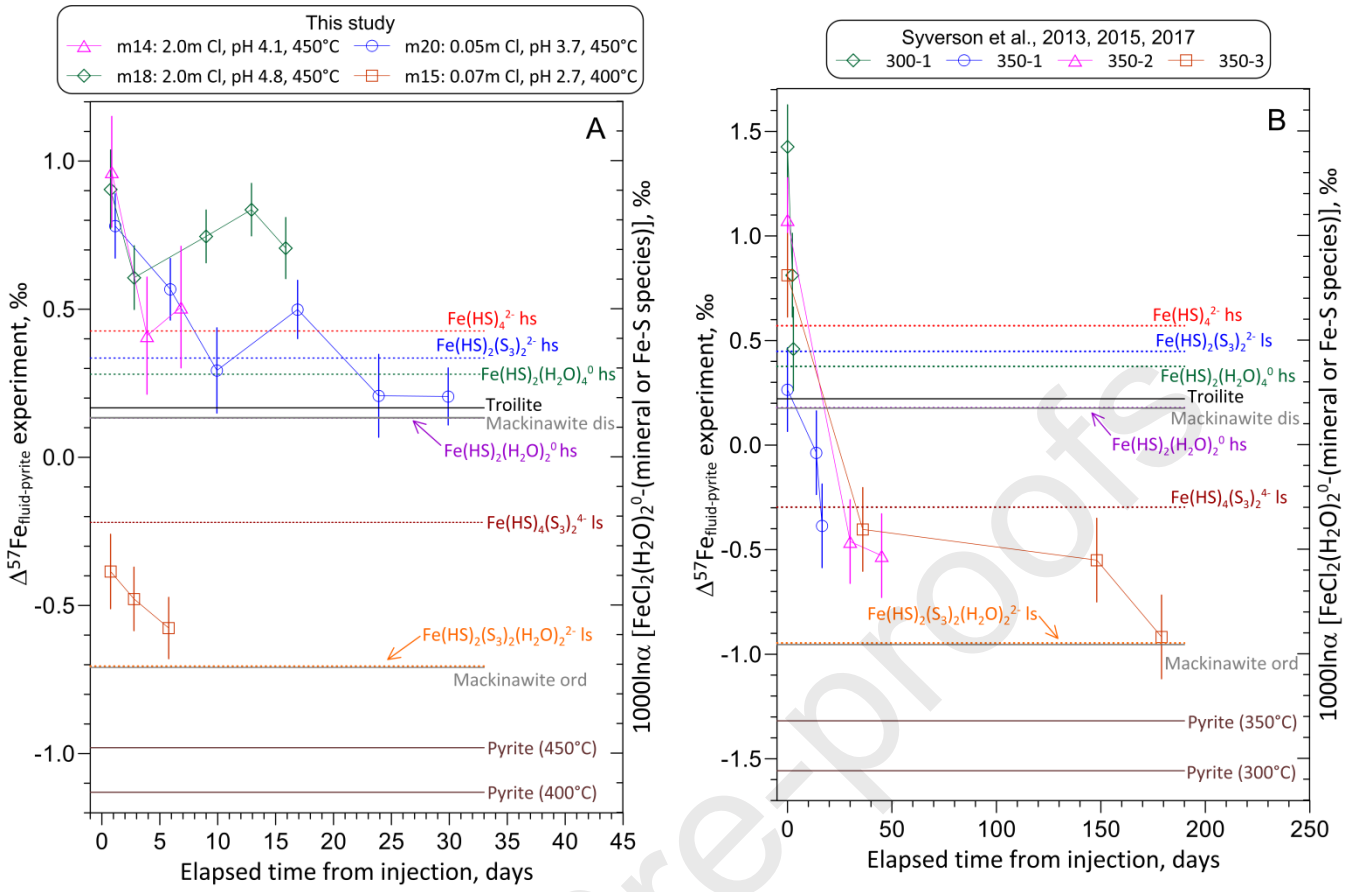

Figure 5. Iron isotope fractionation (expressed as $\Delta^{57}Fe_{fluid\text{-}pyrite}$) between hydrothermal fluid and pyrite measured in this work (A) and available previous studies indicated (B) as a function of time (symbols). For comparison are superimposed predicted fractionations between the dominant $FeCl_2(H_2O)_2^0$ aqueous species and the indicated selected Fe sulfide aqueous complexes (dashed lines) and minerals (solid lines), expressed as the difference of the corresponding theoretical β-factors at 450°C calculated in this study using DFT approaches (see eq. 8, section 2.4). Magnetic spin (hs = high, ls = low) is indicated for each aqueous Fe sulfide species. Mackinawite ord = ordered structure; Mackinawite dis = disordered structure. A two-stage kinetic pattern in the experimental $\Delta^{57}Fe$ vs time is apparent for our runs in (A) (m14, m18, m20) and the longest runs in (B) (350-2 and 350-3), with a fast and short initial stage followed by a longer and slower second stage. Note that chemical fluid-pyrite equilibration (in terms of bulk aqueous Fe concentration) in Syverson et al.'s experiments was attained within <1 day, whereas isotopic equilibrium between the $FeCl_2$-dominated fluid and pyrite was not reached even after 190 days of reaction. Note also that the calculated DFT values for the same species and minerals in (A) and (B) are shifted due to temperature differences.

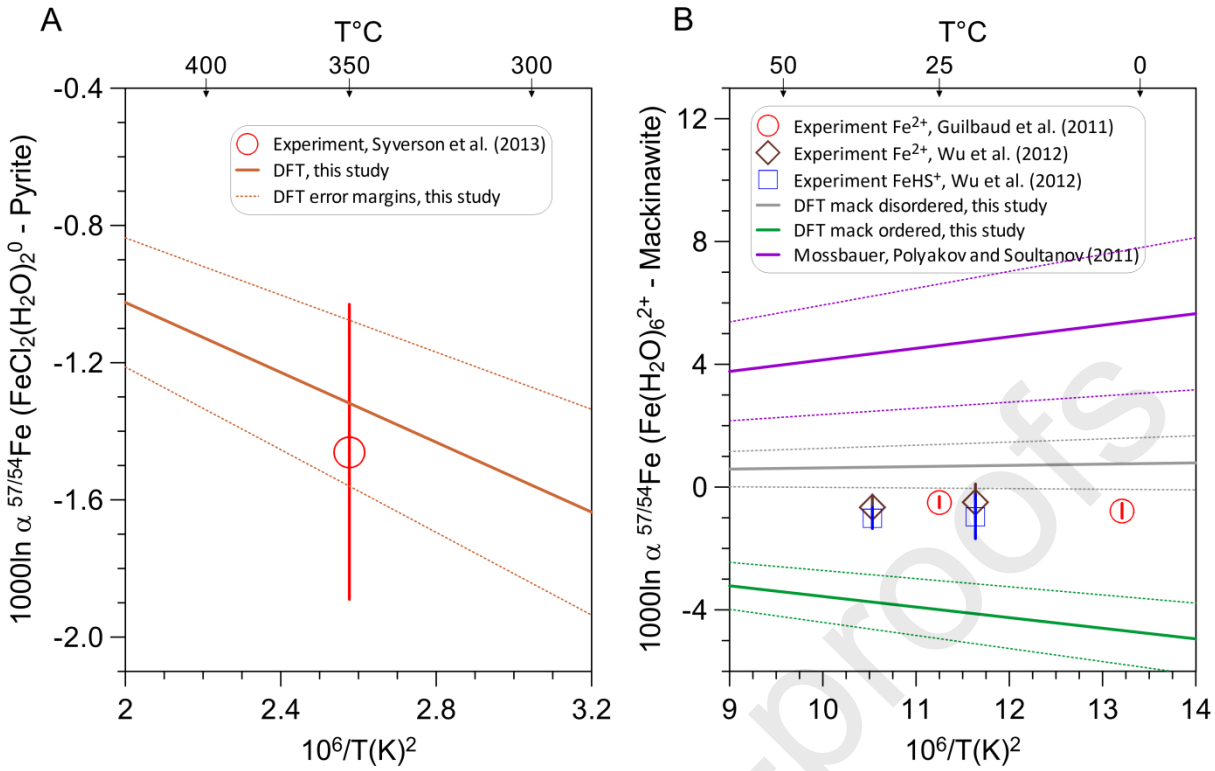

Figure 6. Equilibrium Fe isotope fractionation between the aqueous Fe(II) dichloride complex $FeCl_2(H_2O)_2^0$ and pyrite at hydrothermal conditions (A), and between the aqueous $Fe(H_2O)_6^{2+}$ cation and mackinawite at ambient conditions (B). Experimental results (Syverson et al., 2013; Guilbaud et al., 2011; Wu et al., 2012) are compared with DFT theoretical predictions of this study. In (A) the solid theoretical curve (with its uncertainty margins shown by dotted lines) was obtained by combining the β-factors of aqueous $FeCl_2(H_2O)_2^0$ derived in this study and of pyrite from Blanchard et al. (2009). In (B) the solid theoretical curves (with their dotted error margins) were obtained by combining the calculated Fe^{2+} β-factor with that of ordered and disordered mackinawite generated by DFT calculations of this study or of a mackinawite sample from the Mössbauer spectroscopy derived estimation of Polyakov and Soultanov (2011). An experimental value of fractionation factor between the $FeHS^+$ aqueous complex and mackinawite (Wu et al., 2012) is also shown for comparison (B).

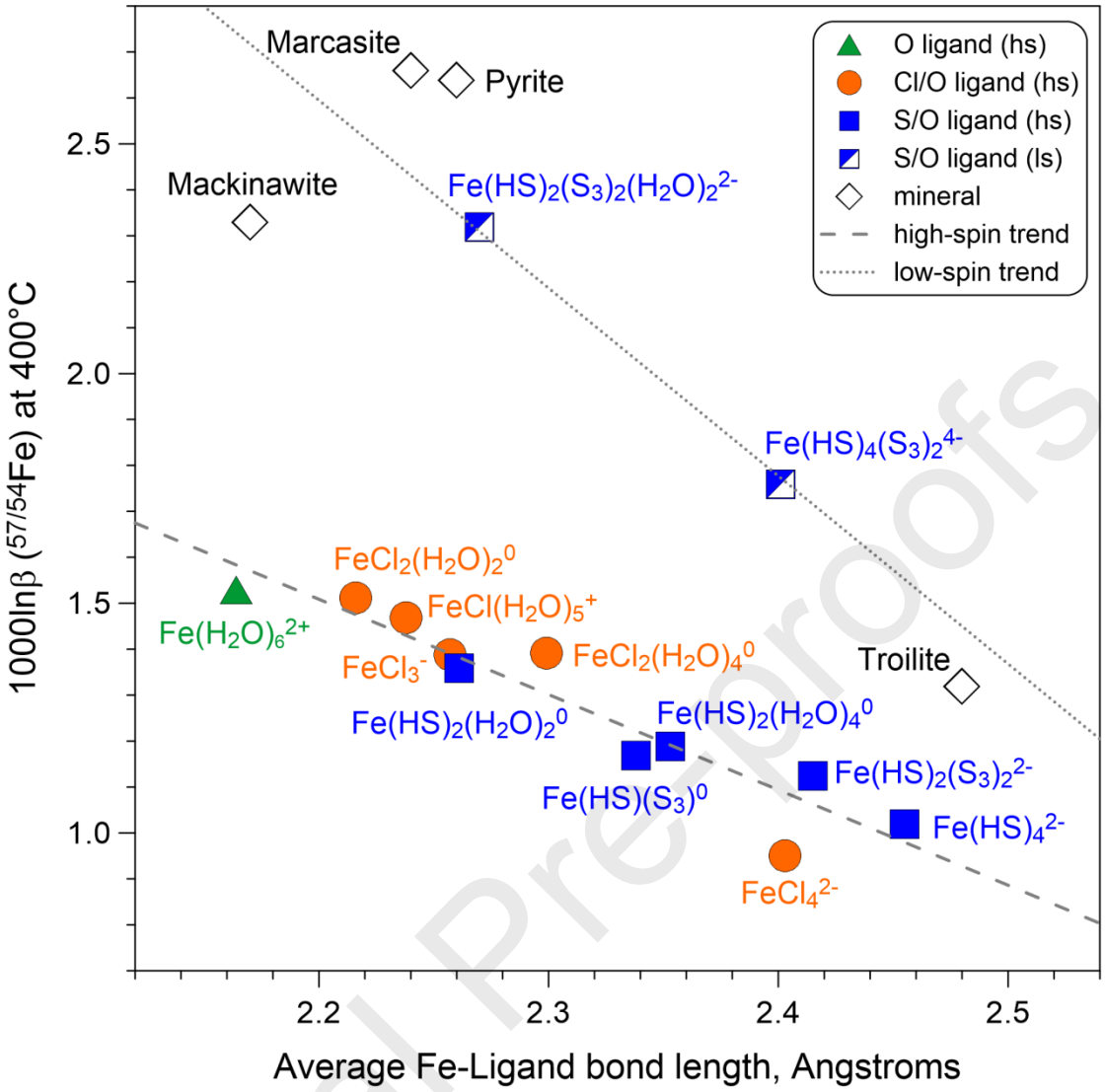

Figure 7. Values of β-factors of $^{57}Fe/^{54}Fe$ (in ‰) at 400°C as a function of the average bond length (in Å) between Fe and its first-shell ligands (L = O, Cl and/or S) in the indicated aqueous complexes and minerals with their respective Fe magnetic spins (ls=low, hs=high), calculated using quantum chemistry methods in this study. The dashed and dotted gray lines are linear regression through Fe high-spin species (lower trend) and low-spin species plus minerals (upper trend), respectively.

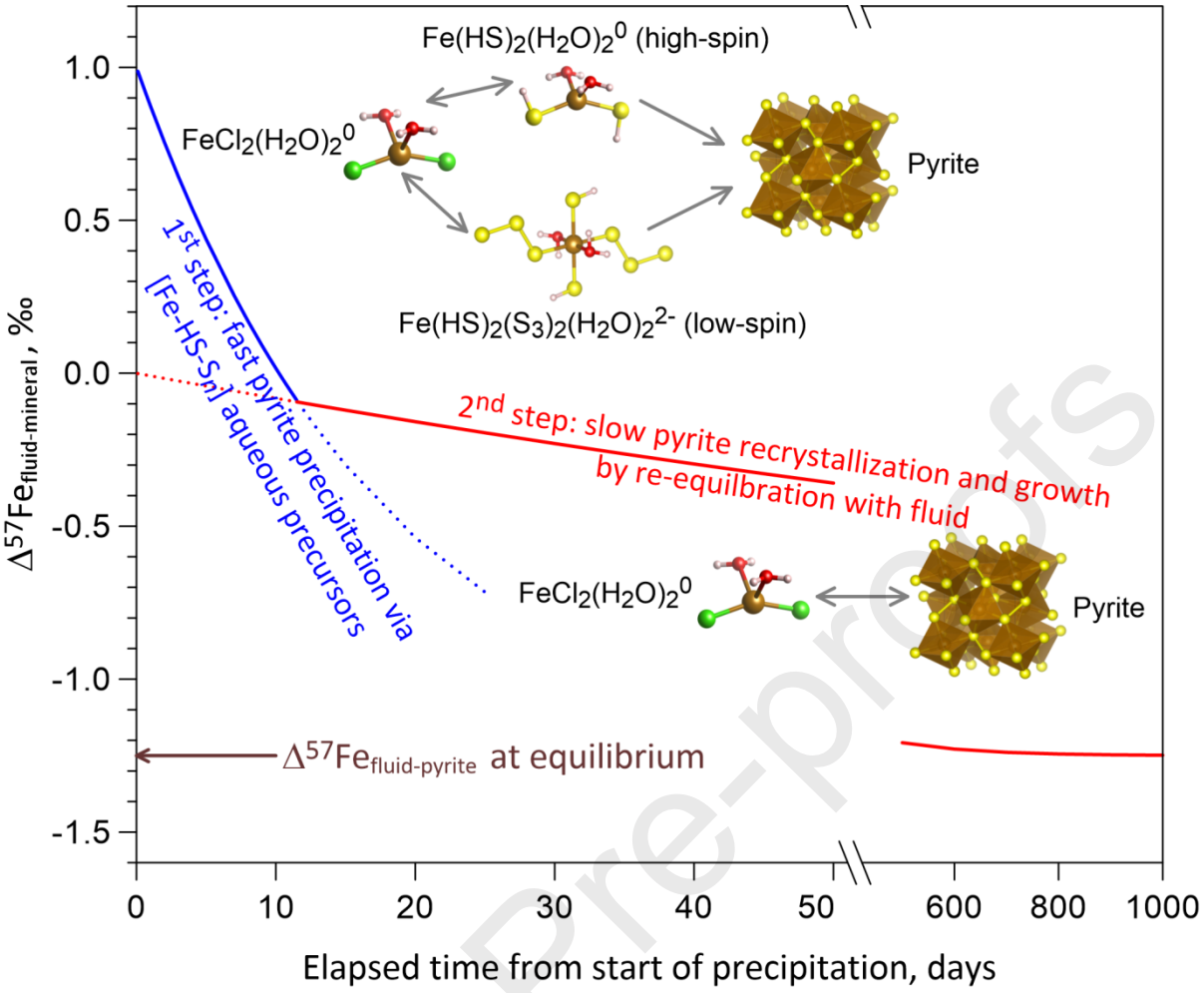

Figure 8. Two-step mechanism of pyrite formation and equilibration between the mineral and hydrothermal fluid controlled by Fe(II) aqueous species, revealed by Fe isotopes in this study at 400–450°C and from analyses of literature data in the *T* range of 300–450°C. Note the X-axis break at >50 days to enable better visualization. The first, both short and fast (<10 days), step of pyrite precipitation (shown by the solid blue curve and its dotted extrapolation to longer durations) occurs via aqueous Fe(II) (poly)sulfide species precursors (e.g., those exemplified here) of stoichiometry, coordination and magnetic spin (low vs high) depending on the fluid composition. These species have Fe isotope signatures corresponding to equilibrium with the dominant Fe(II) di-chloride complex in the fluid. Due to fast formation, the resulting pyrite inherits the isotope composition of those S-bearing species. Depending of the exact precursor species, the resulting pyrite Fe isotope composition is generally by 0.5 to 1.5‰ ^{57}Fe-depleted than that corresponding to equilibrium fractionation between pyrite and the saline fluid dominated by the $FeCl_2(H_2O)_2^0$ complex (indicated by horizontal arrow for the mean value between 300 and 450°C). The second, much slower and longer (100s to 1000 days), step of Fe isotope equilibration with the fluid (solid red curve broken at ~50 days and its dotted interpolation to shorter time) likely occurs through slower pyrite recrystallization and re-equilibration with the fluid and requires about 1 year to reach 90% of Fe isotope equilibrium even at such elevated temperatures.

Table 1. Summary of the experiments conducted in this study and predicted chemical speciation in the aqueous fluid at equilibrium [a].

Run/samples	Experimental bulk aqueous system composition at each step (number of moles of substance per kg fluid, m)	*T*, °C	*P* mean, bar	duration of step, days	Injected aqueous solution	Fe phase formed	pH [b]	fO_2 rel. HM [c]	SI (S^0) [d]	Cl_{tot}, m	H_2S, m	SO_2, m	$\sum SO_4$, m [e]	$S_3^{\bullet-}$ + $S_2^{\bullet-}$, m [f]
m14/1-3	NaCl(1.50), KCl(0.51), NaOH(0.10), S(0.50), ZnS(0.013), CuS(0.015), QMA[g]	450	624	18	-	-	4.1	0.3	-0.45	2.0	0.35	0.12	0.036	0.0094
m14/4-6	$FeCl_2$(0.091), NaCl(1.17), KCl (0.39), NaOH(0.078), S(0.39), ZnS(0.01), CuS(0.01), QMA	450	614	7	$FeCl_2$	pyrite	4.1	0.6	-0.61	1.9	0.20	0.09	0.027	0.0026
m15/1-3	S(0.60)	400	673	8	-	-	2.5	1.2	0.071	0	0.35	0.17	0.004	0.0008
m15/4-6	$FeSO_4$(0.069), S(0.48), NaCl(0.068), H_2SO_4(0.0008)	400	617	7	$FeSO_4$	pyrite	2.7	1.5	-0.12	0.07	0.20	0.22	0.014	0.0007
m18/1-2	NaCl(0.96), KCl(1.00), NaOH(0.06), S (0.55), QMM[g]	450	746	6	-	-	4.8	0.3	-0.53	2.0	0.38	0.04	0.10	0.053
m18/3-6	$FeSO_4$(0.045), NaCl(0.96), KCl(1.00), NaOH(0.05), S(0.49), QMM	450	731	13	$FeSO_4$	pyrite	4.8	0.5	-0.62	2.0	0.26	0.04	0.12	0.023
m18/7	$FeSO_4$(0.036), NaCl(0.96), KCl(1.00), NaOH(0.04), S(0.38), $ZnCl_2$(0.002), $CuCl_2$(0.002), QMM	450	747	3 -	NaCl-KCl	pyrite	4.8	0.5	-0.70	2.0	0.20	0.02	0.10	0.020
m18/9-10 vapor-liquid	$FeSO_4$(0.036), NaCl(0.96), KCl(1.00), NaOH(0.04), S(0.38), $ZnCl_2$(0.002), $CuCl_2$(0.002), QMM	450	410	5	-	pyrite	-	-	-	2.0	-	-	-	-
m20/1-4	NaCl(0.050), S(0.54)	450	753	16	-	-	3.5	0.5	-0.37	0.05	0.36	0.17	0.005	0.0022
m20/5-10	$FeSO_4$(0.025), NaCl(0.05), S(0.51)	450	729	30	$FeSO_4$	pyrite	3.6	0.6	-0.43	0.05	0.29	0.19	0.006	0.0016
error (1SD)	-	±2 °C	±20 bar	-	-	-	±0.1	±0.1	±0.03	±2%	±5%	±10%	±10%	±50%

See Table B.1 for details on measured fluid chemical composition and Table 2 for Fe isotope composition.

[a] Calculated using thermodynamic properties of aqueous species discussed in section 2.3; Fe dominant species is predicted to be $FeCl_2^0$.

[b] Calculated pH of the supercritical fluid at each step at indicated *T*-*P*-composition. For comparison, calculated pH of the neutrality point of water at indicated *T*-*P* (pH^0) is in the range 5.7-6.3 (calculated as $pH^0 = a[H^+] = a[OH^-] = 0.5 \times \log_{10} K_w$, where $K_w = 1/(a_{H+} \times a_{OH-})$ is the water dissociation constant and *a* is H^+ or OH^- ion activity).

[c] Oxygen fugacity in the system (in $\log_{10}$ units) relative to that of the conventional Hematite-Magnetite (HM) mineral redox buffer.

[d] Sulfur saturation index SI (S^0) = $\log_{10}(m_{S(i)}/m_{Ssat})$, where $m_{S(i)}$ is molal concentration of dissolved sulfur at *T*-*P*-composition of step (i), and m_{Ssat} is the apparent saturation concentration for liquid sulfur at step (i). When SI>0, the fluid is saturated with S^0 (liq) whose concentration in the system is reported instead of SI (in m15/1-3).

[e] Sum of sulfate-type species including SO_4^{2-}, HSO_4^- and their ion pairs with Na^+ and K^+.

[f] Concentrations of $S_3^{\bullet-}$ (expressed in moles of S) are typically 10 times more than that of $S_2^{\bullet-}$ at the given *T*-*P*-pH conditions.

[g] QMA and QMM are, respectively, Quartz-Muscovite-Andalusite and Quartz-Muscovite-Microcline mineral assemblages.

Table 2. Iron isotope ratios ($\delta^{57}Fe$ in ‰ relative to IRMM-014) in the coexisting hydrothermal fluid and pyrite, and fluid-pyrite fractionation factor ($\Delta^{57}Fe_{fluid\text{-}pyrite}$, equation 7) derived in this study.

Experiment/sample	days after injection	$\delta^{57}Fe_{fluid}$	2SE[a]	$\delta^{57}Fe_{pyrite}$	2SE[b]	% of Fe in pyrite	$\Delta^{57}Fe_{fluid\text{-}pyrite}$	2SE[b]
m14, injected Fe solution	0	0.477	0.075	-	-	-	-	-
4	0.9	0.908	0.079	-0.06	0.17	44.7	0.96	0.19
5	3.9	0.665	0.091	0.25	0.18	53.7	0.41	0.20
6	6.8	0.719	0.099	0.21	0.18	57.0	0.51	0.21
				Apparent steady-state of stage 1 (5-6)			*0.46*	*0.22*
Pyrite recovered	-	-	-	0.257	0.055	-	-	-
m15, injected Fe solution	0	0.987	0.066	-	-	-	-	-
4	0.8	0.730	0.064	1.12	0.11	66.6	-0.39	0.13
5	2.8	0.537	0.080	1.01	0.07	97.5	-0.48	0.11
6	5.8	0.443	0.075	1.02	0.07	97.5	-0.58	0.10
Pyrite recovered	-	-	-	1.148	0.062	-	-	-
m18, injected Fe solution	0	0.987	0.048	-	-	-	-	-
3	0.8	1.498	0.059	0.59	0.12	56.5	0.90	0.13
4	2.8	1.381	0.042	0.77	0.10	68.2	0.61	0.11
5	9.0	1.557	0.032	0.81	0.08	81.2	0.75	0.09
6	12.9	1.624	0.044	0.79	0.08	82.5	0.84	0.09
7	15.9	1.453	0.068	0.75	0.08	76.4	0.71	0.10
				Apparent steady-state of stage 1 (4-7)			*0.72*	*0.14*
9 vapor	21.0	1.434	0.042	-	-	75.0	-	-
9 liquid	21.0	1.307	0.092	-	-	75.0	-	-
Pyrite recovered	-	-	-	NA	NA	-	-	-
m20, injected Fe solution	0	0.949	0.084	-	-	-	-	-
5	1	1.607	0.040	0.83	0.10	84.2	0.78	0.11
6	6	1.414	0.025	0.85	0.10	86.1	0.57	0.10
7	10	1.187	0.112	0.89	0.09	93.8	0.29	0.14
8	16	1.395	0.039	0.90	0.09	97.5	0.50	0.10
				Apparent steady state of stage 1 (6-8)			*0.45*	*0.15*
9	24	1.111	0.107	0.90	0.09	99.0	0.21	0.14
10	30	1.108	0.034	0.90	0.09	99.1	0.21	0.10
Pyrite recovered	-	-	-	0.765	0.050	-	-	-

[a] Iron isotope composition (in $\delta^{57}Fe$) in the sampled fluid and recovered pyrite and the associated standard error uncertainties defined at 95% probability level (2SE) are calculated from the number of analyses MS-ICPMS (n=4 to 6) and using the Student's t-correction factors (Platzner, 1997).

[b] The corresponding $\delta^{57}Fe$ values of precipitated pyrite at each sampling moment are derived using mass and isotope balance and its error (2SE) is estimated through error propagation (see Appendix C for details). Note a good agreement between the calculated $\delta^{57}Fe$ values of pyrite at the last sampling session and those directly measured in pyrite recovered after the experiment. NA = not available. '-' = not applicable.

Table 3. Polynomial fits of $^{57}Fe/^{54}Fe$ β-factors as a function of temperature for minerals and aqueous species, $1000\ln\beta = ax + bx^2$ with $x = 10^6/T^2$ (T in K), and tabulated $1000\ln\beta$ values at the temperatures relevant to this study.

Mineral or aqueous species	Fe coord[c]	magnetic spin[d]	a	b×10^{-3}	25°C	300°C	400°C	450°C
Pyrite[a]	6	l	1.2054	-4.09	13.05	3.63	2.64	2.29
Marcasite	6	l	1.2122	-4.14	13.13	3.65	2.66	2.30
Mackinawite	4	h	1.0636	-4.00	11.47	3.20	2.33	2.02
Mackinawite disordered[b]	4	h	0.6182	-1.42	6.78	1.87	1.36	1.18
Troilite	6	h	0.6003	-1.22	6.60	1.82	1.32	1.14
$Fe(H_2O)_6^{2+}$	6	h	0.6990	-3.16	7.47	2.10	1.53	1.33
$FeCl(H_2O)_5^{+}$	6	h	0.6713	-3.00	7.18	2.02	1.47	1.27
$FeCl_2(H_2O)_4^{0}$	6	h	0.6357	-2.64	6.82	1.91	1.39	1.21
$FeCl_2(H_2O)_2^{0}$	4	h	0.6913	-3.17	7.38	2.08	1.51	1.31
$FeCl_3^{-}$	3	h	0.6339	-2.30	6.85	1.91	1.39	1.20
$FeCl_4^{2-}$	4	h	0.4325	-0.79	4.77	1.31	0.95	0.82
$Fe(HS)_2(H_2O)_4^{0}$	6	h	0.5431	-2.35	5.82	1.63	1.19	1.03
$Fe(HS)_2(H_2O)_2^{0}$	4	h	0.6211	-2.78	6.64	1.87	1.36	1.18
$Fe(HS)_4^{2-}$	4	h	0.4646	-1.18	5.08	1.40	1.02	0.88
$Fe(HS)(S_3)^{0}$	3	h	0.5341	-2.19	5.74	1.61	1.17	1.01
$Fe(HS)_2(S_3)_2^{2-}$	4	h	0.5127	-1.37	5.60	1.55	1.13	0.98
$Fe(HS)_2(S_3)_2(H_2O)_2^{2-}$	6	l	1.0636	-5.16	11.32	3.19	2.32	2.02
$Fe(HS)_4(S_3)_2^{4-}$	6	l	0.8052	-2.68	8.73	2.43	1.76	1.53

[a] Pyrite β-factors were taken from Blanchard et al. (2009) and correspond to the result obtained from the raw phonon frequencies (no scaling factor).

[b] Fe β-factors of disordered mackinawite are a rough estimation made by applying a scaling factor to the DFT frequencies of crystalline mackinawite, and by using these corrected frequencies in equation (9) (see Appendix A for details).

[c] Fe nearest coordination, 4=tetrahedron, 6=octahedron, 3=triangle.

[d] l=low spin, h=high spin.

Declaration of interests

☒ The authors declare that they have no known competing financial interests or personal relationships that could have appeared to influence the work reported in this paper.

☐The authors declare the following financial interests/personal relationships which may be considered as potential competing interests: